Numerical modeling of the dynamics of bubble oscillations subjected to fast variations in the ambient pressure with a coupled level set and volume of fluid method

Indrajit Chakraborty*
Department of Mechanical Engineering, Technion-IIT, Haifa 32000, Israel
and Mathematics Institute, University of Warwick, Coventry CV4 7AL, United Kingdom

(Received 31 October 2018; published 23 April 2019)

A numerical method for modeling and understanding the dynamics of bubble oscillations subjected to fast variations in the ambient pressure is proposed under low Mach number conditions. In the present work, the method uses a single-fluid continuum formalism of weakly compressible axisymmetric Navier-Stokes equations for the numerical simulation of liquid-gas flows with surface tension and adopts the interface capturing approach based on a coupled level set and volume of fluid (CLSVOF) method for describing the moving and deformed interfaces. To demonstrate the efficacy of the proposed method, first, the numerical results of the radial oscillations of a spherical gas bubble are tested with the numerical solutions of Rayleigh-Plesset equation. Then, the numerical method is applied to reproduce the growth and subsequent collapse of a bubble in an infinite liquid medium observed in experiments. Finally, the numerical simulation of the interaction of two oscillating bubbles at small separation distance is evaluated in response to a moderate step change in the ambient pressure. It is shown that two deformable bubbles undergo coupled radial and oscillatory translational motions which eventually results in the bubbles' attraction and coalescence caused by the secondary Bjerknes forces. The numerical predictions show very good accuracy with the experimental and numerical results reported in the literature.

DOI: 10.1103/PhysRevE.99.043107

I. INTRODUCTION

It is well known that a single gas bubble immersed in liquids exhibits spherical [1,2] or nonspherical volume oscillations [1,3–5] in response to imposed variations in the ambient pressure. In addition to the bubble volume oscillations, spherical and nonspherical bubble collapse may take place as a result of cavitation implosion [1,2,6,7] in a liquid medium depending upon the amplitude of the imposed pressure waves. This collapse may lead to the development of a high-speed re-entrant jet and subsequently the bubble breaks into smaller sized tiny bubbles resulting in the formation of foam [8,9]. Research into this bubble collapse has been generally associated with the problem of cavitation erosion where the undesirable damage of a solid boundary in hydrodynamic systems [2,6,10] can be observed. Nowadays, the study of bubble oscillations and bubble collapse (cavitation) problems has attracted considerable interest in the context of research on biomedical and engineering sciences. Examples include in ultrasonic cleaning and sonochemistry [11], in medical ultrasound fields involving ultrasound contrast agents (UCAs) such as medical sonography [12] and drug delivery systems [13], and many others [14]. A reliable numerical model for the simulation of multiphase flows by considering compressible or weakly compressible liquid-gas flows is of great importance to provide understanding of the phenomena of bubble dynamics involved in these problems. Moreover, it is often required as a viable computational tool to complement both theory and experiment.

With the high speed and significant capacity of the computational resources over the last decades, numerical investigation of two-fluid flows with compressibility or weak compressibility effects still continues to pose a big challenging task and plays an active subject of scientific research for the development of a numerical method [15,16]. The main challenges in simulating the interaction of fast variations in the ambient pressure with a bubble comprise the following treatments: (i) the volume changes of the gas region inside the bubble in a low Mach number regime, (ii) the conservation of mass and momentum, (iii) the exact position of the evolving liquid-gas with a sharp interface, (iv) the high variation of the fluid physical properties such as density and viscosity across the interface (for instance, the density ratio of liquid to gas $\sim$1000), (v) the surface tension forces at the interface, and (vi) topological changes such as coalescence and breakup. The intent of this paper is to deliver a promising and reliable numerical strategy with a coupled level set and volume of fluid method for achieving the mentioned challenges, allowing the numerical simulations of weakly compressible two-phase flows under low Mach number conditions. Then, the numerical results of the dynamics of bubble oscillations in response to the variations in the ambient pressure are shown to prove the validity and accuracy of the proposed numerical approach.

Conventional numerical approaches to study the volume and shape oscillations of a single bubble or two bubble dynamics have been mostly carried out using the boundary integral method (BIM) [10,17–21]. Most of these authors studied the dynamics of a single bubble collapse (cavitation)

*indracster@gmail.com; indrac@technion.ac.il

or bubble-bubble interactions near a solid boundary. The advantage of the BIM is to reduce the order of the governing equations by a factor of 1 which dramatically saves computational time. However, these methods are limited to either potential flows or Stokes flows, and in cases of topological changes it necessitates different numerical techniques. Liu *et al.* [22] used the boundary-fitted finite-volume techniques on a boundary-fitted orthogonal curvilinear coordinate system to simulate the behavior of an oscillating encapsulated bubble dynamics in an ultrasound field. However, these techniques are restricted to capture weak deformations of bubble. An alternative numerical approach for simulating flows with moving interfaces is the so-called arbitrary-Lagrangian-Eulerian (ALE) method proposed by Chatzidai *et al.* [23] and Chatzidai, Dimakopoulos, and Tsamopoulos [24]. In the ALE method, the nodes of the moving, unstructured, and finite element mesh conform to the moving boundary or interface. They applied the ALE method to intensively study the interactions of two oscillating bubbles with shape deformations and translational motions in a quiescent, unbounded incompressible viscous liquid subjected to a step change in the ambient pressure. The ALE method, however, becomes challenging when the moving interface is complex and undergoes large deformations. Moreover, it requires continuous remeshing for the case of large deformations.

Other promising and robust numerical methods for the computation of bubble oscillations in response to the ambient pressure variations using the interface-tracking (front-tracking method) approach and the interface-capturing approach (a coupled level set and volume of fluid method) were presented by several authors. Popinet and Zaleski [25] used a front-tracking (FT) method based on a finite volume formulation. They presented the numerical study of a single bubble collapse and associated liquid jet formation near a solid wall. Hao and Prosperetti [26] proposed a three-dimensional FT finite-difference formulation for tracking free surface and utilized the ghost fluid method (GFM) [27] for handling the pressure jump conditions at the interface. Moreover, a velocity extrapolation numerical technique of Popinet and Zaleski [25] was used near the interface. The method was applied to validate the free oscillation of a spherical gas bubble and the dynamics of an oscillating gas bubble in liquid due to imposed sinusoidal liquid flow. In the framework of the FT method, the interface is tracked explicitly by a moving grid, and the interface position is constructed in a Lagrangian manner using a set of marker points. The advantage of this method is to produce accurate numerical results by maintaining a sharp interface at the cost of complexity. However, difficulties arise when breakup or merging of the interfaces occurs. In contrast to the mentioned FT method, a coupled level set and volume of fluid (CLSVOF) method with adaptive mesh refinement on two-dimensional (2D) axisymmetric coordinate system was introduced by [28]. They showed the numerical simulations of a spherical vapor bubble oscillations and the growth and collapse of a vapor bubble near a solid wall. In the CLSVOF method, as previously proposed by Sussman [28], Sussman and Puckett [29], Gerlach *et al.* [30], Chakraborty, Biswas, and Ghoshdastidar [31], a combined level set (LS) and volume of fluid (VOF) method is employed in a Eulerian framework in order to exploit the advantages of both approaches. With the LS method [32], the interface is represented by a zero contour of a continuous smoothed signed distance function. Thus, it provides a big advantage to compute accurately the interface geometric properties (the interface normal and the curvature) and the surface tension effects. With the VOF method [33], the mass conservation is improved significantly using a mass conserving volume fraction advection of the interface. Additionally, with this coupled method, there is no need to employ any additional numerical strategy for handing the topological change. The present work extends the incompressible CLSVOF method as previously proposed by Chakraborty, Biswas, and Ghoshdastidar [31], in which the method is well validated for the rise and shape of rising bubbles in liquids.

In most of the above mentioned numerical methods for simulating the problem of bubble volume oscillations, the problem is treated as a single-phase flow instead of solving two-phase flow. In their methods, the ambient liquid phase is considered incompressible. The computation of fluid flow only in the liquid side is obtained by solving the Navier-Stokes equations, and a time varying spatially uniform distribution of the gas pressure inside the bubble is considered. The boundary conditions such as pressure and shear stress conditions are imposed on the free surface to examine the effect of gas in the incompressible liquid. In these methods, the gas pressure is computed from the instantaneous bubble volume V obtained from a polytropic law of compression [1]. This effort reduces considerably the cost of computational time and produces reasonably accurate results in a low Mach number regime. Although, it is still limited due to the fact that (i) for the cases of highly deformed interfaces and the collapse of a bubble, the dealing with boundary conditions at the interface is crucial for obtaining accurate numerical solutions and it is strongly dependent on the interface locations and orientations on each two-phase grid cell or interface nodes, and (ii) the fluid flow and the effect of density changes in the gas region are neglected in response to variations in the ambient pressure. Moreover, neglecting the dynamics of fluid flow in the gaseous region might be appropriate in some particular applications. Thus, it is a requisite to present a robust numerical method for solving the full Navier-Stokes equations in both gas and liquid phases in a coupled way under low Mach number conditions.

Recently, Daru *et al.* [34] have proposed a two-phase flow solver based on a single-field finite difference formulation of Navier-Stokes equations combined with energy equation. In [34], the liquid phase is strictly treated as incompressible, while the gas phase is considered compressible with low Mach number approximation. The Lagrangian front tracking method is adopted for tracking the moving interface motion. In the method, a single-fluid two pressure model is used, in which the pressure is split into two components: time varying thermodynamic pressure and hydrodynamics pressure. The method is validated by computing an oscillating water column and is implemented to compute the oscillations of multiple gas bubbles embedded in a closed cavity filled with liquid. Additionally, they have presented that their numerical method is more efficient than a single pressure-based all-Mach method [35,36]. However, the handling of thermodynamic pressure is not straightforward and becomes complex to exactly estimate

it near the interface with the two pressure model. Another kind of method based on the two-phase flow formulation of a weakly compressible volume of fluid (VOF) approach with pressure-projection method is developed by Heyns *et al.* [37]. The method contains a single-fluid Eulerian finite volume approach of Navier-Stokes equations in low Mach number conditions. In the VOF approach for capturing sharp interface of immiscible liquid-gas flows, a color function identifying the volume fraction of the liquid phase is advected using a blended higher-order scheme for mass conservation exactly. It is noteworthy from their newly developed formulation that the resulting advection equation for the volume fraction of liquid is similar to the incompressible two-phase flow VOF formulation. The accuracy and efficiency of their numerical methodology is demonstrated by simulating one-and two-dimensional test cases such as the expansion and compression of gas. However, the surface tension effects are not taken into account in their model. Furthermore, it is noteworthy that the methods developed in [34,37] have not further been extended to the problems of the pressure driven oscillating gas bubble system when it is strongly deformed. Most recently, Huber *et al.* [38] and Duret *et al.* [39] have proposed a compressible two-phase flow solver for the numerical simulation of low Mach number liquid-gas flows with surface tension effects using the LS method and the CLSVOF method, respectively. Huber *et al.* [38] have performed the numerical simulation of the interaction of ultrasound waves with a bubble without considering the viscous effects. With the phase change model, Duret *et al.* [39] have presented the numerical results of the vaporization process inside the two-phase flow homogeneous isotropic turbulence (HIT) configuration. In [39], the density and viscosity are calculated based on the liquid and gas volume fractions in a single-fluid formulation. However, the calculations of the discontinuous physical properties from volume fractions sometimes may lead to numerical instabilities near the interface [29].

This work, which pursues the idea of the aforementioned numerical works [34,37], presents a numerical method based on a single-fluid approach of weakly compressible axisymmetric Navier-Stokes equations for the numerical simulation of bubble oscillations in response to pressure variations in the ambient liquid. The method uses the interface capturing procedure based on the CLSVOF algorithm [31] to compute the interface motion. The surface tension effects at the interface are handled by a continuous surface force (CSF) model developed by Brackbill, Kothe, and Zemach [40]. In this numerical method combined with a pressure-based algorithm [34,35,39], the numerical solution to the governing equations is performed using a Eulerian finite difference framework. For the sake of simplicity, the pressure inside the gas bubble is considered to depend solely on the gas density through the equation of state (EOS). In particular, the equation of state of the gas is modelled with a polytropic law of compression [1].

The remainder of the paper is organized as follows. In Sec. II, the problem is formulated and the details concerning the governing equations and the numerical methodology are presented. In Sec. III, three different test problems are presented in order to strengthen the relevance of the proposed numerical method. First, the numerical results of the radial oscillations of a spherical bubble are validated with the numerical solutions of Rayleigh-Plesset equation. Next, the growth and collapse of a bubble subjected to expansion and compression pressure waves and the associated formation of the re-entrant liquid jet are shown. The prediction of the time history of the equivalent bubble radius is compared with the experimental results of Rodríguez-Rodríguez, Casado-Chacón, and Fuster [9]. Finally, the interactions between bubble pairs in response to a step change in the ambient pressure are computed. The accuracy of the computed results is assessed by comparisons with the numerical results of Chatzidai *et al.* [23]. The simulations of the interaction of two oscillating bubbles seem to be initiated by using the present weakly compressible two-phase flow solver coupled with interface capturing procedure. Moreover, in this section, some qualitative results of the time evolution of bubble shapes are given. In order to characterize the dynamics of bubble shapes, a quantitative measure of the bubble aspect ratio $\beta = \frac{d_z}{d_r}$ is used, where d_z and d_r are the vertical and horizontal extremes of the bubble, respectively. Finally, the concluding remarks are stated in Sec. IV.

II. FORMULATION OF THE PROBLEM

A. Problem description

The geometry of the problem under study is shown in Fig. 1 for the purpose of modeling numerically the dynamics of oscillating bubbles immersed in a liquid of density ρ_l and viscosity μ_l subjected to fast variations in the ambient pressure p_∞. To study this problem computationally, an axisymmetric configuration in cylindrical coordinates (r, z, θ) is chosen as sketched in Fig. 1(a) where a single gas bubble of radius R, density ρ_g, and viscosity μ_g is located with its center on the symmetric axis of the computational geometry. Here, (r, z, θ) are the radial, axial, and azimuthal coordinates, respectively. In this study, the problem is assumed to be independent of θ, and the effects of gravity are neglected. The subscripts l and g denote the liquid and gas phases, respectively.

B. Governing equations

1. Gas phase

The most commonly used continuity equation for compressible flows in the pure gas phase [see Fig. 1(a)] can be written as follows:

$$\frac{\partial \rho_g}{\partial t} + \nabla \cdot (\rho_g \mathbf{v}) = 0, \tag{1}$$

which results in

$$\nabla \cdot \mathbf{v} = -\frac{1}{\rho_g}\frac{D\rho_g}{Dt}, \tag{2}$$

where $\frac{D}{Dt}(= \frac{\partial}{\partial t} + \mathbf{v} \cdot \nabla)$ is the material derivative, $\mathbf{v} = (u, v)$ is the velocity vector with u and v standing for radial and axial components of the velocity vector, and t is the time. Note that for the case of incompressible gas phase the above simply reads as $\nabla \cdot \mathbf{v} = 0$. In order to close Eq. (1) an equation of state (EOS) is required, and density as a function of pressure is considered solely. For this purpose, the thermodynamic equation known as the isentropic equation for the sound speed

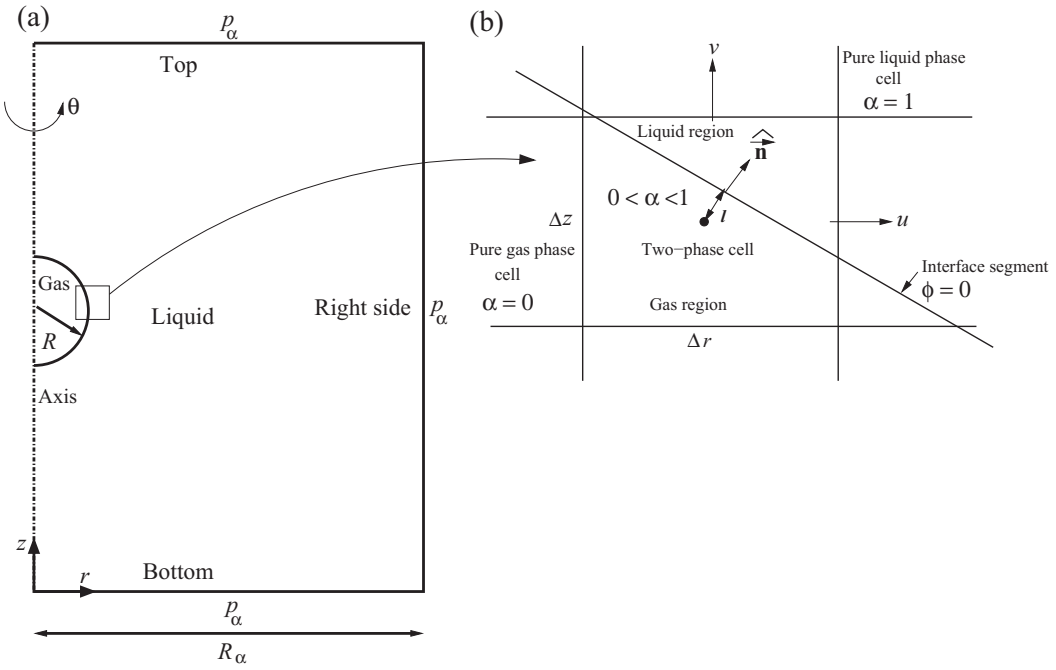

FIG. 1. (a) Schematic diagram of the problem geometry and axisymmetric computational domain on a (r, z) plane used to model the behavior of a single gas bubble oscillations due to changes in the ambient pressure p_∞. (b) Computational two-phase cell with piecewise-linear interface segment and distribution of volume of liquid fraction α around the interface. The width and height of the computational domain are denoted as R_∞ and L_∞ (see in Sec. II D), respectively.

in gas can be used as

$$c_g = \sqrt{\frac{\partial p}{\partial \rho_g}}. \tag{3}$$

For an ideal gas, the sound speed is given by

$$c_g = \sqrt{\frac{\gamma_g p}{\rho_g}}, \tag{4}$$

where p is the pressure and γ_g is the polytropic index with $\gamma_g = 1$ and 1.4 for isothermal and adiabatic motion of gas bubble, respectively. Finally, the continuity Eq. (2) for the compressible gas phase can be rewritten as follows:

$$\nabla \cdot \mathbf{v} = -\frac{1}{\rho_g c_g^2}\frac{Dp}{Dt} = -\frac{1}{\gamma_g p}\frac{Dp}{Dt}. \tag{5}$$

Moreover, by incorporating Eq. (3) into Eq. (1), the following pressure equation is obtained:

$$\frac{\partial p}{\partial t} + \mathbf{v}\cdot\nabla p + \rho_g c_g^2 \nabla\cdot\mathbf{v} = 0, \tag{6}$$

where $\rho_g c_g^2 = K_g$ is the compressibility parameter of the gas phase known as the bulk modulus of elasticity. Note that in the above equation the second term is the convection of pressure and the last term is the production of pressure due to volume change.

Using the initial bubble radius, $R_{\text{ref}} = R_0$, as the length scale, the initial atmospheric pressure, $p_{\text{ref}} = p_{\text{atm}}$, as the pressure scale, $U_{\text{ref}} = \sqrt{\frac{p_{\text{atm}}}{\rho_{l,\text{ref}}}}$ as the velocity scale, and $t_{\text{ref}} = R_0\sqrt{\frac{\rho_{l,\text{ref}}}{p_{\text{atm}}}}$ as the time scale, Eq. (6) is cast in dimensionless form as follows:

$$\frac{M_g^2}{\rho_g^*}\frac{\partial p^*}{\partial t^*} + \frac{M_g^2}{\rho_g^*}\mathbf{v}^*\cdot\nabla^* p^* + \nabla^*\cdot\mathbf{v}^* = 0, \tag{7}$$

where the reference pressure, density, and velocity are $p_{\text{ref}} = 10^5$ Pa, $\rho_{l,\text{ref}} = 10^3$ kg m^{-3} and $U_{\text{ref}} = 10$ m s^{-1}. As a result, the gas Mach number $M_g = \frac{U_{\text{ref}}}{c_g}$ and the term $\rho_g^* = \frac{\rho_g}{\rho_{l,\text{ref}}}$ become of the order 10^{-2} and 10^{-3}, respectively, in the present study. Here, the * denotes the normalized quantity. It can be noted that for a weakly compressible gas phase system (for small M_g, i.e., $M_g \ll 1$), the first and second terms of Eq. (7) might not be dropped out.

As reported before by Prosperetti, Crum, and Commander [41], the ratio of the maximum pressure difference in the bubble Δp to the gas pressure p is given by

$$\frac{\Delta p}{p} = O\left(\frac{M_b R(t)}{\lambda_g}, M_b^2\right),$$

where $R(t)$ is the instantaneous radius of the gas bubble, $M_b(=\frac{\dot{R}}{c_g})$ refers to the Mach number of the bubble wall motion defined as the ratio of the bubble wall velocity $\dot{R}(t) = \frac{dR}{dt}$ to the speed of sound in gas c_g, and the wavelength λ_g corresponds to the speed of sound in the gas. When both $\frac{R(t)}{\lambda_g}$ and M_b are sufficiently smaller than unity the gas pressure inside the bubble is considered to be uniform spatially and only function of time. For the sake of simplicity, it is, therefore, allowable to drop the second term of Eq. (7). However, considering uniform gas pressure inside the bubble is not pertinent to computing the interaction of a bubble with pressure waves

(shock waves) when the Mach number is high [37,38]. It is worth noting that the first term cannot be neglected, as in the case of fast variations of the ambient pressure with high frequency and very short time scales resulting in the rapid volume and shape oscillations of gas bubbles in liquid. Therefore, from the foregoing analysis, Eq. (6) for weakly compressible gas flows can be written as follows:

$$\frac{1}{\rho_g c_g^2}\frac{\partial p}{\partial t} = -\nabla\cdot\mathbf{v}, \tag{8}$$

which finally reads as

$$\frac{1}{\gamma_g p^0}\frac{dp^0}{dt} = -\nabla\cdot\mathbf{v}. \tag{9}$$

In Eq. (8), $p(\mathbf{x},t)$ denotes a unique (single) pressure which itself contains both the time varying thermodynamic pressure $p^0(t)$ and the hydrodynamic pressure $p^2(\mathbf{x},t)$; see [34] for more details. Here, $\mathbf{x}=(r,z)$ is the position vector. The thermodynamic pressure is considered uniform spatially in the gas phase and depends on the EOS. On the other hand, the hydrodynamic pressure is responsible for the satisfaction of the continuity equation for the gas phase. Based on the asymptotic analysis [34,38], the hydrodynamic pressure is sufficiently smaller than the thermodynamic pressure when $M_g \to 0$. As a consequence, it can be noted from Eq. (9) that $p(\mathbf{x},t)$ is replaced by $p^0(t)$, which is relevant for a weakly compressible gas flow system. It is worth noting that the term appearing in the left-hand side of Eq. (9) is related to the isentropic expansion and compression of the gas bubble in a low Mach number regime.

The conventional approach to the investigation of the oscillations of a gas bubble in response to changes in the ambient pressure is that the gas pressure inside the bubble follows the polytropic equation of state [1,41], which writes

$$\rho_g = \rho_{g,\mathrm{ref}}\left(\frac{p}{p_{g,\mathrm{ref}}}\right)^{1/\gamma_g}, \tag{10}$$

where $p_{g,\mathrm{ref}}$ is the initial equilibrium pressure inside the bubble with the initial atmospheric reference pressure p_{atm} and $\rho_{g,\mathrm{ref}}$ is the reference gas density corresponding to $p_{g,\mathrm{ref}}$.

By considering compressible flow, the momentum equation for the gas phase in conservative form can be written as

$$\frac{\partial(\rho_g\mathbf{v})}{\partial t} + \nabla\cdot(\rho_g\mathbf{v}\mathbf{v}) = -\nabla p + \nabla\cdot\left[\mu_g(\nabla\mathbf{v}+\nabla\mathbf{v}^T) - \tfrac{2}{3}\mu_g(\nabla\cdot\mathbf{v})\mathbf{I}\right],$$

where $\mathbf{I}$ is the identity tensor.

2. Liquid phase

In a similar way [see Eq. (1)], the continuity equation for compressible flow in pure liquid phase can be presented as

$$\frac{\partial\rho_l}{\partial t} + \mathbf{v}\cdot\nabla\rho_l + \rho_l\nabla\cdot\mathbf{v} = 0. \tag{11}$$

Using the isentropic relation for the speed of sound in liquid, $c_l = \sqrt{\frac{\partial p}{\partial\rho_l}}$, Eq. (11) leads to the following equation:

$$\frac{\partial p}{\partial t} + \mathbf{v}\cdot\nabla p + \rho_l c_l^2\nabla\cdot\mathbf{v} = 0, \tag{12}$$

where the term $\rho_l c_l^2 = K_l$ is the compressibility parameter of the liquid phase. For the liquid phase, the Tait equation of state, $p = B(\frac{\rho_l}{\rho_{l,\mathrm{ref}}})^{\gamma_l} - B + p_{\mathrm{atm}}$, can be used in order to close Eq. (12). Here, γ_l is the adiabatic index for the liquid with $\gamma_l = 7$ and the constant $B = 3.31\times10^8$ Pa. From the Tait equation, the speed of sound in liquid can be expressed as

$$c_l = \sqrt{\frac{\gamma_l B}{\rho_{l,\mathrm{ref}}}\left(\frac{\rho_l}{\rho_{l,\mathrm{ref}}}\right)^{\gamma_l-1}}.$$

Now, Eq. (12) can be further expressed in dimensionless form by using the aforementioned mentioned reference scales, and the following equation is obtained:

$$\frac{M_l^2}{\rho_l^*}\frac{\partial p^*}{\partial t^*} + \frac{M_l^2}{\rho_l^*}\mathbf{v}^*\cdot\nabla^* p^* + \nabla^*\cdot\mathbf{v}^* = 0, \tag{13}$$

where, $M_l = \frac{U_{\mathrm{ref}}}{c_l}$ is the liquid Mach number which is of order 10^{-3}, and the dimensionless term $\rho_l^* = \frac{\rho_l}{\rho_{l,\mathrm{ref}}}$ is of order unity. It can be reasonable that for a weakly compressible flow with low Mach number liquid system under the study (for very small M_l with $M_l^2 \sim 10^{-6}$), the first and the second terms of Eq. (13) can be dropped out [37]. Finally, the continuity Eq. (11) for the liquid phase can be rewritten as

$$\nabla\cdot\mathbf{v} = 0. \tag{14}$$

The above analysis allows us to consider that the ambient liquid phase is incompressible fluid [34,37] with constant density. Therefore, the momentum equation for the motion of weakly compressible flow in liquid phase under the present study is similar to that of incompressible fluid flow, which can be represented in conservative form as follows:

$$\frac{\partial(\rho_l\mathbf{v})}{\partial t} + \nabla\cdot(\rho_l\mathbf{v}\mathbf{v}) = -\nabla p + \nabla\cdot[\mu_l(\nabla\mathbf{v}+\nabla\mathbf{v}^T)].$$

3. Single-fluid formulation and governing equations

In a single-fluid continuum approach, both the liquid and gas phases are treated as a single fluid with variable physical properties. In this approach, a single continuity equation and a single momentum equation can be used taking the corresponding fluid physical properties in each phase. Moreover, this approach enables us to a continuous velocity field around the interface. With the CLSVOF method, based on the above analysis, the governing equations for the weakly compressible single-fluid formulation can be expressed as

$$\nabla\cdot\mathbf{v} = -\frac{(1-\alpha)}{\gamma_g p}\frac{Dp}{Dt}, \tag{15}$$

$$\frac{\partial(\rho\mathbf{v})}{\partial t} + \nabla\cdot(\rho\mathbf{v}\mathbf{v}) = -\nabla p + \nabla\cdot\left[\mu(\nabla\mathbf{v}+\nabla\mathbf{v}^T) - \frac{2}{3}\mu(\nabla\cdot\mathbf{v})\mathbf{I}\right] + \mathbf{f}_{st}, \tag{16}$$

$$\frac{1-\alpha}{\gamma_g p^0}\frac{dp^0}{dt} = -\nabla\cdot\mathbf{v}, \tag{17}$$

where ρ and μ are the density and viscosity, respectively. For gas-liquid two-phase systems, α and $1-\alpha$ are defined as the

liquid volume fraction and the gas volume fraction occupied in each cell. In a single-fluid model, the continuity Eqs. (15) and (17) are obtained from Eqs. (5) and (9), respectively. Note that Eqs. (15) and (17) are valid for a pure weakly compressible gas phase cell ($\alpha = 0$), a pure incompressible liquid phase cell ($\alpha = 0$), and a two-phase cell ($0 < \alpha < 1$). In the momentum Eq. (16), which accounts for surface tension effects, the term $\mathbf{f}_{st}$ is incorporated as the surface tension force per unit volume [40] and it is expressed as

$$\mathbf{f}_{st} = \sigma\kappa\,\vec{\mathbf{n}}\,\delta_s,$$

which leads to

$$\mathbf{f}_{st} = \sigma\kappa\mathbf{n},$$

where σ is the surface tension coefficient assumed to be constant, κ is the local curvature of the interface, δ_s is the surface delta function which takes 1 at the interface and 0 elsewhere, and $\vec{\mathbf{n}}$ and $\mathbf{n}$ are the unit normal vector and the normal vector, respectively, at the interface directed outward to the liquid phase. Following the CLSVOF method [29,31], the momentum transport Eq. (16) can be rewritten in a non-conservative form as follows:

$$\left(\frac{\partial \mathbf{v}}{\partial t} + \mathbf{v}\cdot\nabla\mathbf{v}\right) = -\frac{1}{\rho(\zeta)}\nabla p + \frac{1}{\rho(\zeta)}\nabla\cdot\Big[\mu(\zeta)(\nabla\mathbf{v} + \nabla\mathbf{v}^T) - \frac{2}{3}\mu(\zeta)(\nabla\cdot\mathbf{v})\mathbf{I}\Big] + \frac{1}{\rho(\zeta)}\sigma\kappa\nabla\zeta, \quad (18)$$

where $\mathbf{n}$ is calculated from

$$\mathbf{n} = \nabla\zeta.$$

Here, ζ is a smoothed Heaviside function $H_\epsilon(\phi)$ as used elsewhere [29,31] and defined as

$$\zeta = H_\epsilon(\phi) = \begin{cases} 0 & \text{if } \phi < -\epsilon \\ 1 & \text{if } \phi > \epsilon \\ \frac{1}{2} + \frac{\phi}{2\epsilon} + \frac{1}{2\pi}\left[\sin\left(\frac{\pi\phi}{\epsilon}\right)\right] & |\phi| \leqslant \epsilon, \end{cases} \quad (19)$$

where ϕ is the level set function defined as a signed-distance function $\phi(\mathbf{x}, t)$ [32]. The function $\phi(\mathbf{x}, t)$ represents the shortest distance measured from a nearby grid point $\mathbf{x}$ to the interface at time t. It is set to be zero ($\phi = 0$) at the interface and takes negative values in the gas phase and positive values in the liquid phase. In the CLSVOF method, $H_\epsilon(\phi)$ is used to compute the normal vector at the interface for the consistent calculation of surface tension force per unit volume [see Eq. (18)]. In addition, the single-fluid formulation also allows us to calculate the mixture density $\rho(\zeta)$ and viscosity $\mu(\zeta)$ using $H_\epsilon(\phi)$ in the entire domain:

$$\rho(\zeta) = \zeta\rho_l + (1-\zeta)\rho_g, \quad (20)$$

$$\mu(\zeta) = \zeta\mu_l + (1-\zeta)\mu_g, \quad (21)$$

where ρ_l, μ_l, and μ_g are constant. Furthermore, in Eq. (19), the control parameter 2ϵ represents the finite interface thickness. Our experience shows [31] that the typical values of ϵ vary from one to four times the length of the smallest size of the computational cell. In the present work, $\epsilon = 3.5\Delta r$ is chosen in order to reduce nonphysical flow (spurious currents) around the interface significantly and achieve the realistic bubble shapes when the surface tension force is dominant. Here, Δr denotes the size of the computational cell. Considering the spurious currents, it generates due to the imbalance of surface tension force resulting to the numerical instabilities around the interface. One of the major reasons for this instability is due to inaccurate curvature (κ) estimation. In the CLSVOF method proposed by Sussman and Puckett [29], the accurate estimations of the interface unit normal vector $\vec{\mathbf{n}}$ and the local interface curvature κ are computed using a level set function ϕ as

$$\vec{\mathbf{n}} = \frac{\nabla\phi}{|\nabla\phi|}, \quad (22)$$

and

$$\kappa(\phi) = -\nabla\cdot\left(\frac{\nabla\phi}{|\nabla\phi|}\right). \quad (23)$$

For the axisymmetric case (r, z), Eq. (23) can be expressed as

$$\kappa = -\frac{\phi_z^2\phi_{rr} - 2\phi_r\phi_z\phi_{rz} + \phi_r^2\phi_{zz}}{\left(\phi_r^2 + \phi_z^2\right)^{3/2}} - \frac{\phi_r}{r\left(\phi_r^2 + \phi_z^2\right)^{1/2}}, \quad (24)$$

where the subscripts r and z denote the first derivative with respect to r or z. Equations (22) and (24) are discretized using second-order central-differencing schemes for spatial derivatives.

In addition, for a weakly compressible single-fluid flow model, the following advection equations for the volume fraction α (see in Appendix A),

$$\frac{\partial\alpha}{\partial t} + \nabla\cdot(\alpha\mathbf{v}) = 0, \quad (25)$$

and the level set function ϕ,

$$\frac{\partial\phi}{\partial t} + \mathbf{v}\cdot\nabla\phi = 0, \quad (26)$$

are solved to describe the evolution of the interface.

C. Numerical methodologies

In the framework of the method proposed in the current work for the simulation of weakly compressible liquid-gas flows, the governing equations are solved on a uniform Eulerian staggered grid arrangement [42] using the finite difference approach. In a staggered grid arrangement, the scalars $(p,\ \rho, \mu, \alpha, \phi)$ are located at the cell centers, while the velocity components $(\mathbf{v})$ are on the cell faces [see Fig. 1(b)]. The convection terms of Eqs. (18) and (26) are discretized using a second-order essentially nonoscillatory (ENO) scheme [43] and the viscous terms of Eq. (18) are discretized by the central differencing scheme. The fluid variables $\mathbf{v}$ and p are computed by using a prediction-projection algorithm [44]. The overview of the numerical methodology and procedure are now described in more detail by the following steps:

(i) *Time discretization*. First, the continuity equation [Eq. (15)] and momentum equation [Eq. (18)] are discretized in time as

$$\nabla\cdot\mathbf{v}^{n+1} = -\frac{(1-\alpha^n)}{\gamma_g\widehat{p}^0}\left(\frac{Dp}{Dt}\right)^{n+1}, \quad (27)$$

$$\mathbf{v}^{n+1} = -\mathbf{v}^n \cdot \nabla \mathbf{v}^n - \frac{\Delta t}{\widehat{\rho}} \nabla p^{n+1} + \frac{\Delta t}{\widehat{\rho}} \nabla \cdot \left[\mu(\nabla \mathbf{v} + \nabla \mathbf{v}^T) - \frac{2}{3}\mu(\nabla \cdot \mathbf{v})\mathbf{I} \right]^n + \frac{\Delta t}{\widehat{\rho}} \sigma \kappa^n \nabla \zeta^n, \tag{28}$$

where superscripts n ($t^n = n\Delta t$) and $n+1$ [$t^{n+1} = (n+1)\Delta t$] denote the old and new time levels, respectively, and Δt is the time step for the computations. As can be noted, Eq. (28) is discretized with first-order explicit temporal discretization. It is seen from the above equations that $\mathbf{v}^{n+1}$, p^{n+1}, and an intermediate density $\widehat{\rho}$ are unknown.

(ii) *Intermediate thermodynamics gas pressure* $\widehat{p}^0$. Then, $\widehat{p}^0$ from Eq. (17) is calculated as

$$\frac{1}{p^0}\frac{dp^0}{dt} = -\frac{\gamma_g}{\int_V (1-\alpha) dV} \int_V \nabla \cdot \mathbf{v} dV, \tag{29}$$

which results in

$$\widehat{p}^0 = p^{0,n} \exp\left(\int_{t^n}^{\widehat{t}} \frac{1}{p^0}\frac{dp^0}{dt} dt \right), \tag{30}$$

or

$$\widehat{p}^0 = p^{0,n} \exp\left[\frac{3\Delta t}{2}\left(\frac{1}{p^0}\frac{dp^0}{dt}\right)^n - \frac{\Delta t}{2}\left(\frac{1}{p^0}\frac{dp^0}{dt}\right)^{n-1} \right],$$

where $(\frac{1}{p^0}\frac{dp^0}{dt})^n$ and $(\frac{1}{p^0}\frac{dp^0}{dt})^{n-1}$ are calculated from Eq. (29). Time integration of Eq. (30) is performed by using the second-order Adams-Bashforth method. Here, V denotes the volume of the whole computational domain.

(iii) *Intermediate density* $\widehat{\rho}$. After obtaining the value of $\widehat{p}^0$, the gas density $\widehat{\rho_g}$ is determined using the equation of state (10) and the single-fluid density $\widehat{\rho}$ is calculated using (20) through

$$\widehat{\rho} = \zeta^n \rho_l + (1-\zeta^n)\widehat{\rho_g}.$$

(iv) *Projection method*. Next, the predicted velocities $\widetilde{\mathbf{v}}$ from Eq. (18) is computed using the pressure gradient ∇p^n obtained from the old time step as follows:

$$\widetilde{\mathbf{v}} = -\mathbf{v}^n \cdot \nabla \mathbf{v}^n - \frac{\Delta t}{\widehat{\rho}} \nabla p^n + \frac{\Delta t}{\widehat{\rho}} \nabla \cdot \left[\mu(\nabla \mathbf{v} + \nabla \mathbf{v}^T) - \frac{2}{3}\mu(\nabla \cdot \mathbf{v})\mathbf{I} \right]^n + \frac{\Delta t}{\widehat{\rho}} \sigma \kappa^n \nabla \zeta^n.$$

However, this equation still does not satisfy the mass conservation Eq. (27). Then, Eq. (28) is subtracted from Eq. (31), as given by

$$\mathbf{v}^{n+1} - \widetilde{\mathbf{v}} = -\frac{\Delta t}{\widehat{\rho}} \nabla p', \tag{31}$$

taking pressure correction $p' = p^{n+1} - p^n$.

(v) *Helmholtz-type equation.* Operating divergence to Eq. (31), the following equation for the pressure correction is obtained:

$$-\nabla \cdot (\nabla p'/\widehat{\rho}) = \frac{1}{\Delta t}(\nabla \cdot \mathbf{v}^{n+1} - \nabla \cdot \widetilde{\mathbf{v}}), \tag{32}$$

where

$$\nabla \cdot \mathbf{v}^{n+1} = -(1-\alpha^n)\frac{1}{\gamma_g \widehat{p}^0}\left(\frac{Dp}{Dt}\right)^{n+1},$$

which yields

$$\nabla \cdot \mathbf{v}^{n+1} = -(1-\alpha^n)\frac{1}{\gamma_g \widehat{p}^0}\left(\frac{p^{n+1}-p^n}{\Delta t} + \widetilde{\mathbf{v}} \cdot \nabla(p^n + p')\right). \tag{33}$$

Substituting Eq. (33) into Eq. (32) results in the following Helmholtz-type equation for the pressure correction:

$$\nabla \cdot (\nabla p'/\widehat{\rho}) - \left(\frac{1-\alpha^n}{\gamma_g \widehat{p}^0}\right)\frac{1}{\Delta t}\left(\frac{p'}{\Delta t} + \widetilde{\mathbf{v}} \cdot \nabla p'\right) = \left[\frac{1}{\Delta t}\nabla \cdot \widetilde{\mathbf{v}} + \frac{1}{\Delta t}\left(\frac{1-\alpha^n}{\gamma_g \widehat{p}^0}\right)\widetilde{\mathbf{v}} \cdot \nabla p^n\right]. \tag{34}$$

This step ensures the conservation of mass for the whole computational domain. The pressure correction Eq. (34) is solved by an iterative method based on the preconditioned biconjugate gradients stabilized scheme (Bi-CGSTAB) of Van der Vorst [45]. The convergence criterion of this iteration is set for the tolerance value of 10^{-7}.

(vi) *Updated velocities and pressure fields.* Once the pressure correction p' is obtained, the pressure p^{n+1} and velocities $\mathbf{v}^{n+1}$ are determined at a new time level, t^{n+1} given by

$$p^{n+1} = p^n + p', \tag{35}$$

$$\mathbf{v}^{n+1} = \widetilde{\mathbf{v}} - \frac{\Delta t}{\widehat{\rho}} \nabla p'. \tag{36}$$

(vii) *Advections and interface reconstruction*. Based on the velocity field at new time level $\mathbf{v}^{n+1}$, the advection equations (25) and (26) are solved numerically by using a coupled second-order operator split advection algorithm in order to find α^{n+1} and ϕ^{n+1}; see more details on this algorithm in [30,31,46]. In the operator split advection algorithm performed here, the advection equations are split into a series of one dimensional advections in each spatial direction followed by a reconstruction step of the interface. Interface reconstruction is carried out using the least-squares volume-of-fluid interface reconstruction algorithm (LVIRA) of Puckett *et al.* [46] and Pilliod and Puckett [47]. In LVIRA, the interface is approximated in each two-phase cell ($0 < \alpha < 1$) by a piecewise-linear interface segment to know the approximate position of the interface as shown in Fig. 1(b). The position of the interface segment is represented by the unit normal vector $\widehat{\vec{\mathbf{n}}}$ of the approximate interface by using the initial guess of $\vec{\mathbf{n}}$ [see Eq. (22)] and the distance l measured from the center of the computational cell to the approximate interface in such a way that the volume fraction of the approximate interface $\widehat{\alpha}$ matches the actual α obtained after the advection.

(viii) *Reinitialization of* ϕ. During each fractional step of operator split advection algorithm [see in step (vii)], the solution of the advection equation for ϕ [Eq. (26)] will move the zero level set $\phi = 0$ at the interface exactly. However, ϕ fails to keep the signed normal distance property (i.e., $|\nabla \phi| \neq 1$), because the distance function cannot be conserved. This problem will successively result in poor mass conservation. In

order to maintain the distance property of ϕ exactly, one needs to reinitialize ϕ based on the current reconstructed interface by coupling the level set function to the volume fraction. In this work, a reinitialization algorithm proposed by Sussman, Smereka, and Osher [48] and Sussman and Puckett [29] is implemented to retain ϕ as an exact distance function in the region of the interface. It can be done using the following reinitialization equation:

$$\frac{\partial \phi}{\partial \tau} = S(\phi_0)(1 - |\nabla \phi|), \tag{37}$$

where τ is a pseudotime and $S(\phi_0)$ is a smoothed sign function of the level set function $\phi_0 = \phi(\mathbf{x}, \tau = 0)$ defined in [48]. Now, $\phi^{n+1} = 0$ describing the new interface position and ϕ^{n+1} as a correct distance function for next time level are known.

(ix) Repeat step (i) with the new computed $\mathbf{v}^{n+1}$, p^{n+1}, α^{n+1}, and ϕ^{n+1} for the computations of the next time level.

In the present work, the time step Δt is chosen to satisfy Courant-Friedrichs-Lewy (CFL) time condition due to the explicit scheme of the calculations and is restricted in accordance with the criterion

$$\Delta t = \mathrm{CFL}\left(\frac{\Delta r}{|u|_{\max} + |v|_{\max}}\right), \tag{38}$$

which ensures the stability of the solution. Here, $|u|_{\max}$ and $|v|_{\max}$ are the maximum values of the velocities, respectively. In the current work, CFL = 0.25 is used. In addition, the time step Δt is also checked from the stability criterion of viscous and capillary time step conditions as discussed in Chakraborty, Biswas, and Ghoshdastidar [31].

D. Computational domain and boundary conditions

The computational domain established for the axisymmetric simulations of the problems to be considered in this paper is shown in Fig. 1(a). In the present simulations, the computational domain size with dimensions $[r, z] = [0, 16R_0$ or $32R_0][0, 16R_0$ or $32R_0]$ for the case of a single bubble with the initial equilibrium radius of a spherical bubble R_0 is chosen in order to consider the far-field domain.

Here, the symmetry boundary conditions are imposed along the axis of symmetry. The boundary condition for velocities $\mathbf{v}$ and applied driving far-field pressure variations p_∞ on the other boundaries are set to

$$\frac{\partial \mathbf{v}}{\partial n} = 0$$

and

$$p_\infty = \begin{cases} p_{\mathrm{atm}};\ t \leqslant 0 \\ p_{\mathrm{atm}}(1+\varepsilon);\ \text{step change},\ t > 0 \\ p_{\mathrm{atm}}(1 \pm \varepsilon \sin(\omega_f t));\ \text{oscillatory field},\ t > 0, \end{cases} \tag{39}$$

respectively, where n is the unit outward normal on the boundaries, $\varepsilon = \Delta p / p_{\mathrm{atm}}$ is the amplitude of pressure disturbance, $\omega_f = 2\pi f_f$ is the forcing frequency, and p_{atm} is the initial equilibrium pressure in liquid.

The initial condition used for the simulations corresponding to the velocities is zero in the whole computational domain. The initial equilibrium pressure of a single spherical bubble is calculated by ($p_{g,\mathrm{ref}} = p_{\mathrm{atm}} + \frac{2\sigma}{R_0}$).

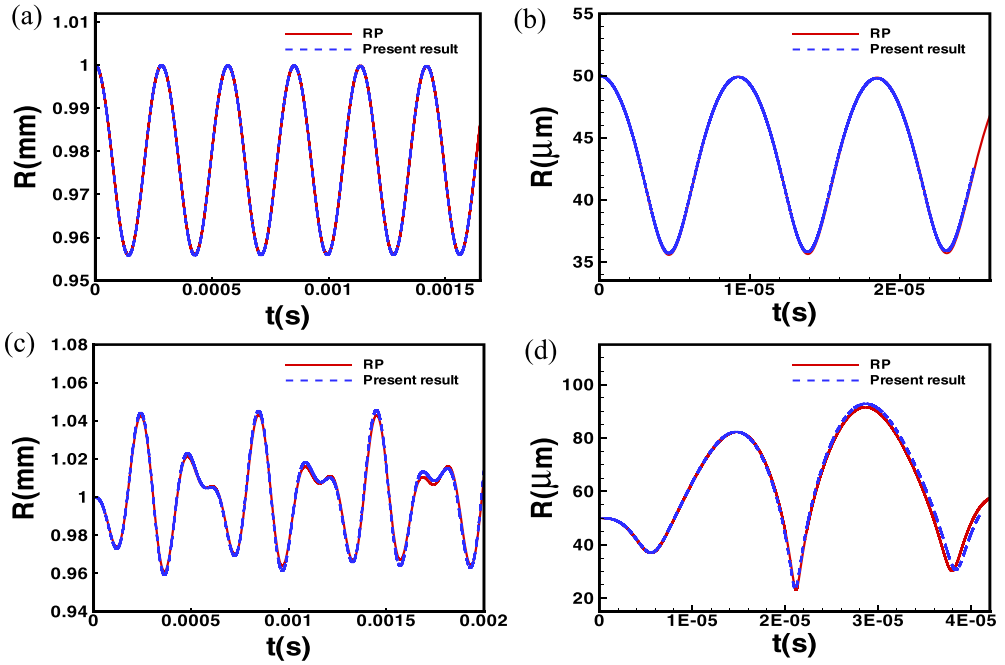

FIG. 2. Comparison of numerically computed radial oscillations of a spherical gas bubble with the numerical solution of RP equation [1] using the parameters (a) $\varepsilon = 10^{-1}$ and $R_0 = 1$ mm, (b) $\varepsilon = 10^{0}$ and $R_0 = 50$ μm, (c) $\varepsilon = 10^{-1}$ and $R_0 = 1$ mm, and $f_f = 5$ kHz, and (d) $\varepsilon = 10^{0}$ and $R_0 = 50$ μm and $f_f = 80$ kHz. The other input parameters taken as follows: $p_{\mathrm{atm}} = 10^5$ Pa, $\rho_l = 1000$ kg m^{-3}, $\rho_{g,\mathrm{ref}} = 1$ kg m^{-3}, $\mu_l = 10^{-3}$ kg m^{-1} s^{-1}, $\mu_g = 10^{-5}$ kg m^{-1} s^{-1}, $\sigma = 0.072$ kg s^{-2}, and $\gamma = 1.4$, with 800 × 800 grid cells.

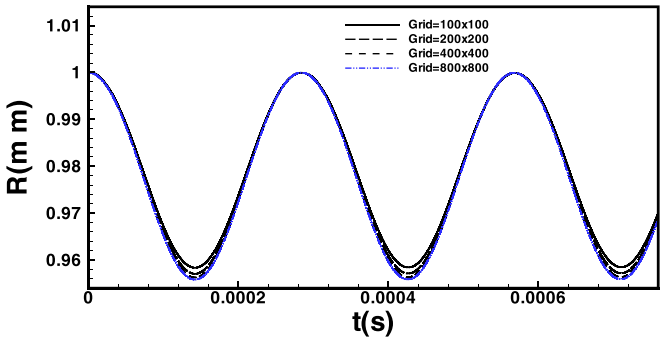

FIG. 3. Effect of computational grid cells on the temporal variation of the spherical bubble radius using the same parameters as in Fig. 2(b).

III. VALIDATION AND RESULTS

The numerical studies of three different problems are conducted to assess the accuracy and the justification of the above numerical approach by simulating the dynamics of a single bubble or two interacting bubbles under the influence of pressure changes in the ambient liquid medium.

A. Spherical bubble oscillation

This validation test considers a spherically oscillating bubble system in liquid. Here, the oscillation is represented in terms of the time evolution of the radius of a spherical bubble subjected to fast variations in far-field ambient pressure. It is well known that the evolution of the radius of a spherical bubble, R, in an incompressible liquid is governed by the Rayleigh-Plesset (hereafter referred to as RP) framework [1]:

$$R\ddot{R} + \frac{3}{2}\dot{R}^2 = \frac{1}{\rho_l}\left(p_g - p_\infty - \frac{2\sigma}{R} - \frac{4\mu_l}{R}\dot{R}\right), \tag{40}$$

where dots represent time derivatives, p_g is the gas pressure related to a polytropic equation, $p_g = p_{g,\mathrm{ref}}(\frac{R_0}{R})^{3\gamma_g}$. The above ordinary differential equation (ODE) can be solved by using the fourth-order Runge-Kutta method. Initially, the radius of a spherical bubble and the bubble wall velocity are assumed to be R_0 (equivalent bubble volume, $V_0 = \frac{4\pi}{3}R_0^3$) and zero [$\dot{R}(t=0) = 0$)], respectively. In order to verify the accuracy of the proposed method, the predictions of the radial dynamics of a spherical bubble are compared with the numerical solutions of RP equation, as shown in Fig. 2. It is observed that the simulation results agree very well with the RP analysis.

Then, a grid refinement study on the evolution of the radius of a spherical bubble for different computational grid cells with CFL = 0.25 is carried out in order to ensure the finest resolution of the current results, as illustrated in Figs. 3 and 4. It is observed from Fig. 3 that by increasing grid cells, a grid convergence is observed and the numerical result approaches closely the numerical solution of the RP equation [see Fig. 2(b)]. In Fig. 4, the numerical results for 200×200 and 400×400 grid cells yield differences on the minimum radius of the spherical bubble ($t = 1.42 \times 10^{-4}$ s) during the first oscillation. In addition, Table I shows the difference of the numerical error on the minimum value of R relative to the solution of RP equation at $t = 1.42 \times 10^{-4}$ s for several grids.

Furthermore, in order to maintain numerical stability of our computational method, it is required to choose the appropriate CFL number based on the numerical stability criterion of CFL $\leqslant 1$. Figure 5 presents the time evolution of the relative error in total mass of gas in the bubble using three different values of CFL number, CFL = 1.0, CFL = 0.5, and CFL = 0.25 with $\Delta r/R_0 = 0.02$ and the same parameters as used in Fig. 2(b). The time evolution of relative total mass error (Δm) is defined by

$$\Delta m = \frac{m_g(t) - m_g(0)}{m_g(0)}, \tag{41}$$

where $m_g(t)$ is the total mass of gas in the bubble at time t. It is observed that for CFL = 0.5 and CFL = 0.25 the maximum amplitudes of the relative gas-mass error are about 1.30×10^{-5} and 6.0×10^{-6} at $t = 1.92 \times 10^{-3}$ s, respectively, while

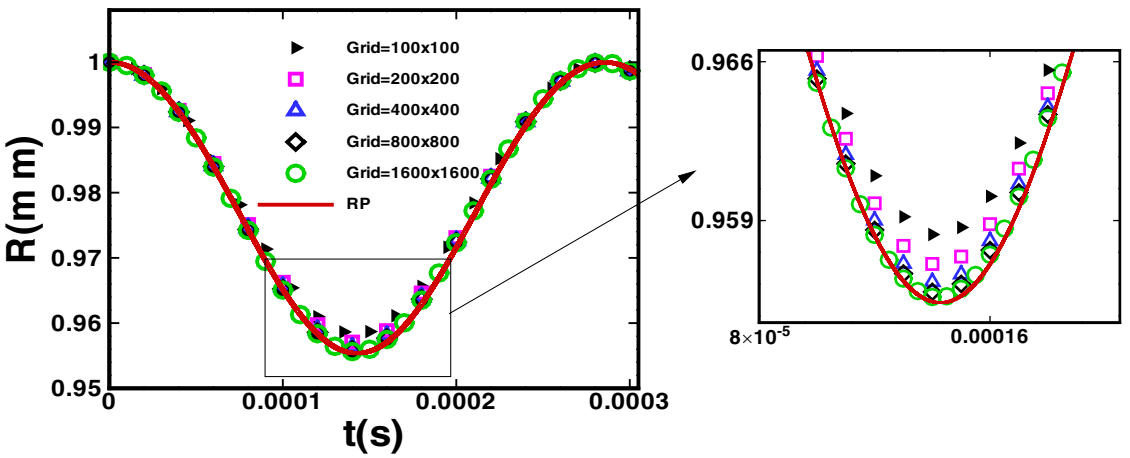

FIG. 4. Effect of grids on the radius profile comparison with RP solution during the first oscillation with the same parameters as in Fig. 2(b). Arrow indicates the zoom view of the variations of the minimum radius for different grids. The minimum radius of the bubble is $R_{\mathrm{min,RP}} = 9.554 \times 10^{-1}$ mm at $t = 1.42 \times 10^{-4}$ s.

TABLE I. Relative error of radius R with $\Delta R = \frac{R_{min,num} - R_{min,RP}}{R_{min,RP}}$ at $t = 1.42 \times 10^{-4}$ s. Here, the subscripts RP and num refer to the values of the minimum radius R_{min} obtained from RP analysis and present numerical results.

Grid cells	Grid size $= \frac{\Delta r}{R_0}$	ΔR
100×100	1.6	3.31×10^{-3}
200×200	0.08	1.75×10^{-3}
400×400	0.04	9.30×10^{-4}
800×800	0.02	4.50×10^{-4}
1600×1600	0.01	2.40×10^{-4}

for CFL = 1.0 it is about 6.3×10^{-5} which is much higher than that obtained from other smaller CFL numbers. The reason for this error may be due to the present reinitialization scheme for the level set function used also for mass conservation. A similar kind of numerical results is reported by Daru *et al.* [34], Duret *et al.* [39], and Huber *et al.* [38] to find the mass loss of air for studying the oscillating water column in the tube and the oscillations of bubble under ultrasound waves, respectively.

Therefore, based on the above numerical results, it clearly demonstrates that the numerical simulations of the dynamics of bubble oscillating in liquid can be carried out by using CFL = 0.25 and $\Delta r/R_0 = 0.02$ in the rest of this paper. Moreover, with grid size 0.02 the total computational time can be saved without compromising the accuracy of the numerical results. Regarding the Mach number in this simulation, the maximum value of the Mach number (M_g) in the gas becomes of the order of 10^{-3} which is much smaller than unity.

Next, the pressure contours with velocity vectors at the first cycle of bubble volume oscillations [see in Fig. 2(b)] is displayed in Fig. 6. It is observed that initially at $t = 5 \times 10^{-7}$ s the surrounding pressure is higher than the internal gas pressure. As a result, fluid flows in the inward direction and the bubble shrinks. The contraction persists in the process which results in an increase to the gas pressure inside the bubble and a decrease of the bubble size. It is seen that at $t = 10^{-4}$ s the gas pressure is higher than that of the surrounding and the bubble contraction still happens because of inertia. The contraction phase continues until the gas pressure inside the bubble becomes sufficiently larger than the surrounding liquid pressure leading to stop the contraction phase at $t = 1.42 \times 10^{-4}$ s and then the expansion phase starts. At the expansion phase at $t = 1.9 \times 10^{-4}$ s, the gas pressure inside bubble is higher than the surrounding pressure and fluid flows in the outward direction resulting in a decrease to the gas pressure. It is observed that at $t = 2.5 \times 10^{-4}$ s, which is before the bubble starts to contract again, the gas pressure inside the bubble is lower than that of the surrounding pressure. However, the inertia causes the bubble to overexpand continuously, and the expansion phase then stops at $t = 2.84 \times 10^{-4}$ s. This process continues until the gas pressure inside the bubble reaches a state of equilibrium with the new ambient pressure. Furthermore, the results show qualitatively that there are no nonphysical flows (spurious currents) [31,38] around the interface obtained from the current method using $\Delta r/R_0 = 0.02$ and CFL = 0.25.

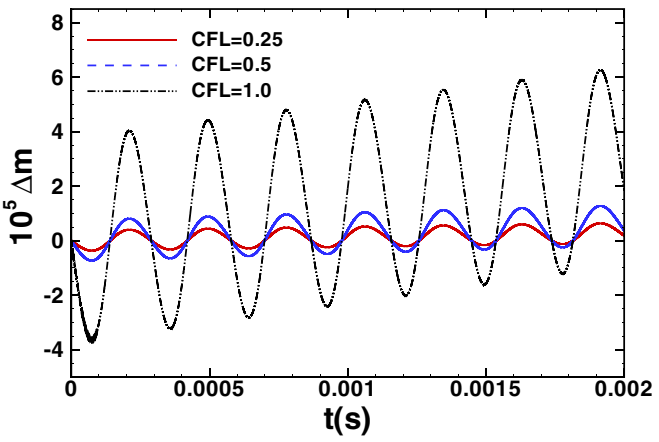

FIG. 5. The time evolution of relative gas-mass error under the same conditions of Fig. 2(b). Black dash-dotted line: CFL = 1.0; blue dash line: CFL = 0.5; red solid line: CFL = 0.25.

B. Collapse of an isolated single bubble in an unbounded liquid medium

In this section, the growth and collapse of an initially spherical gas (CO_2) bubble of radius $R_0 = 180$ μm at equilibrium in water subjected to a sinusoidal pressure forcing of expansion-compression waves [see Fig. 7(a)] is examined. This investigation was carried out experimentally by Rodríguez-Rodríguez, Casado-Chacón, and Fuster [9] to show the bubble collapse interacting with the measured pressure variations following the RP equation. To reproduce this experimental study, the predicted numerical results of the radial dynamics of a bubble during successive expansion-collapse phases are presented in Fig. 7 and compared with the experimental data of Rodríguez-Rodríguez, Casado-Chacón, and Fuster [9]. The input computational parameters corresponding to the experiment are $p_{atm} = 10^5$ Pa, $\Delta p = 10^5$ Pa ($\varepsilon = 1$), $T = 0.24$ ms ($f_f = 4.17$ kHz), $\rho_l = 1000$ kg m^{-3}, $\rho_{g,ref} = 1$ kg m^{-3}, $\mu_l = 10^{-3}$ kg m^{-1} s^{-1}, $\mu_g = 10^{-5}$ kg m^{-1} s^{-1}, and $\sigma = 0.0434$ kg s^{-2}. The polytropic index of gas inside the bubble is $\gamma = 1.304$ defined in [9]. The computations [see also the computational domain in Fig. 1(a)] are performed using 1000×1000 grid cells. In the problem of interest, R_0 can be chosen as a length scale, $R_0\sqrt{\frac{\rho_l}{p_{atm}}}$ as a time scale, and $\sqrt{\frac{p_{atm}}{\rho_l}}$ as a velocity scale.

Figure 7(b) shows the comparison of the time history of the equivalent radius of the bubble between the present computed result, RP solution, and the experimental data. Note that the present computation results and the RP solution are displayed from $t = 0.068$ ms. In experiment, the bubble responds and begins to grow in size at the expansion phase when $t \approx 0.068$ ms. It can be readily seen from Fig. 7(b) that at time between 0.068 ms $\leqslant t <$ 0.21 ms, the present numerical prediction (dashed line) shows a very good agreement with the experimental results (circle symbol) and the RP solution (solid line) during the complete expansion phase of the bubble to its maximum size [see below in Fig. 8(a)] and the collapse phase [from A to near point B in Fig. 7(a)] to its minimum size [see below in Fig. 8(b)]. It is noteworthy from the results that

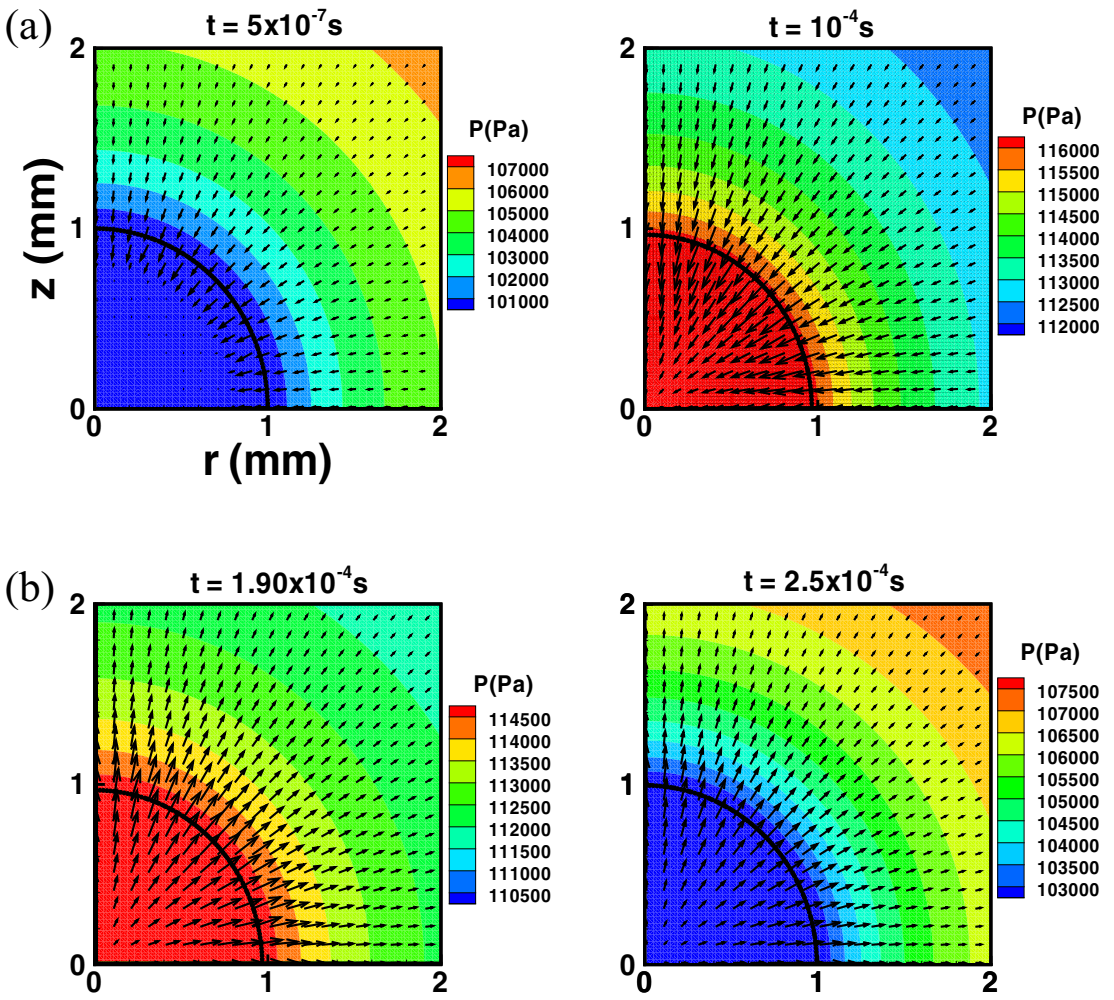

FIG. 6. (a) Pressure distribution with velocity field during first contraction phase. For the first cycle, the time period for contraction phase is $0\ \text{s} \leqslant t \leqslant 1.42 \times 10^{-4}$ s; (b) pressure distribution with velocity field during first expansion phase of a spherical gas bubble. For the first cycle, the time period for expansion phase is $1.42 \times 10^{-4}\ \text{s} < t \leqslant 2.84 \times 10^{-4}$ s. The parameters used here are the same as in Fig. 2(b).

the final stage of the bubble collapse phase ends with a minimum size at $t_{\text{collapse, exp}} \approx 0.22$ ms, $t_{\text{collapse, RP}} = 0.2135$ ms, and $t_{\text{collapse, num}} = 0.2115$ ms and then the bubble rebound phase begins, which also justifies the accuracy of the current numerical framework. Here, t_{collapse} refers to the time for the end stage of the bubble collapse phase, and the subscripts exp, RP, and num denote the values of t_{collapse} obtained from experiment, RP analysis, and simulation, respectively.

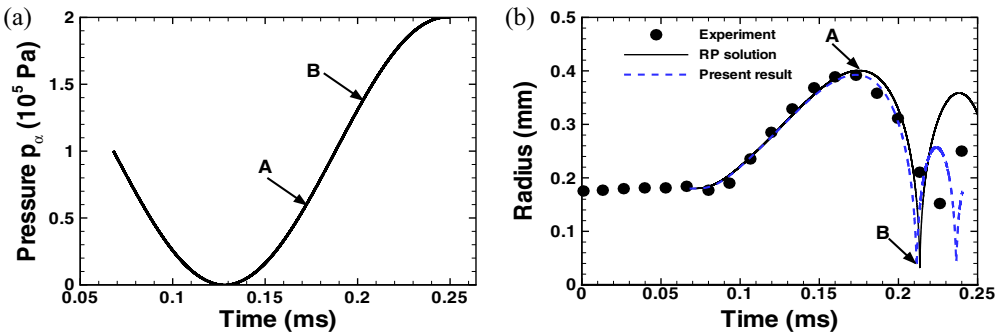

FIG. 7. (a) Imposed oscillatory pressure field at the far boundary and (b) Comparison of the history of the equivalent radius of the bubble between experimental measurements [9], Rayleigh-Plesset equation for oscillating spherical bubble system, and present numerical results. Here, A and B inside the figure refer to the end of first expansion phase with maximum bubble radius and the end of first collapse phase with minimum bubble radius, respectively.

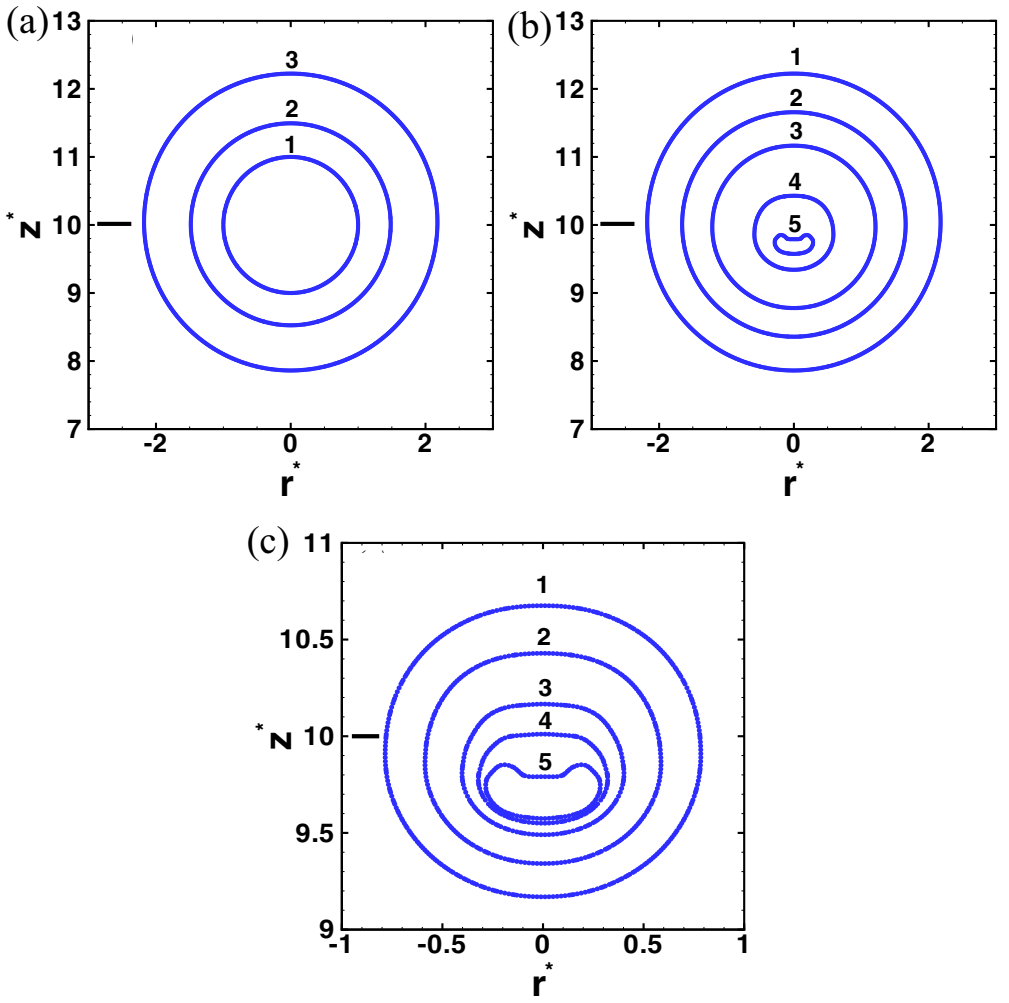

FIG. 8. Snapshots of the time evolution of the bubble shapes during (a) first expansion phase at times t (t^*) (1) 0.0000 ms (0), (2) 0.1165 ms (6.47), (3) 0.1731 ms (9.62); (b) first collapse phase at times t (t^*) (1) 0.1731 ms (9.62), (2) 0.2004 ms (11.13), (3) 0.2066 ms (11.48), (4) 0.2105 ms (11.69), (5) 0.2115 ms (11.75); (c) magnified snapshots of the evolution of the bubble shapes at the final stages of the collapse phase at times t (t^*) (1) 0.2097 ms (11.65), (2) 0.2105 ms (11.69), (3) 0.2111 ms (11.73), (4) 0.2113 ms (11.74), (5) 0.2115 ms (11.75). The bubble reaches the first maximum radius at the end of the expansion phase and the first minimum radius at the end of the collapse phase at $t = 0.1731$ ms or $t^* = 9.62$ and $t = 0.2115$ ms or $t^* = 11.75$, respectively. Note that the horizontal black marks of the left side near vertical axis denote the initial position of the bubble. These black marks indicate the displacement of the bubble center from its initial position. The input parameters are same as used in Fig. 7.

As can be observed from the snapshots of the time evolution of bubble shapes shown in Fig. 8, the bubble shape remains spherical during the entire expansion phase and most of the collapse phase. However, at the final stages of the bubble collapse, the upper surface of the bubble is flattened and the bubble deviates from spherical shape and deforms into an oblatelike-shaped bubble [sequence from 2–4 in Fig. 8(c)]. It is also observed that at the end of collapse phase at $t =$ 0.2115 ms or $t^* = 11.75$ (see sequence 5), the bubble shape becomes a kidneylike-shaped bubble, where t^* refers to the dimensionless time.

The time sequence snapshots of bubble shapes during the early stages of the rebound phase [after collapse phase $t >$ 0.2115 ms ($t^* > 11.75$)] is qualitatively reproduced in the simulation reported in Fig. 9, where the re-entrant liquid jet formed at the end of the bubble collapse phase penetrates through the bubble. Eventually, the re-entrant liquid jet impacts on the lower surface of the bubble [Fig. 9(b)] at $t =$ 0.2119ms ($t^* = 11.77$) and the bubble breaks into a toroidal bubble [Fig. 9(c)]. As time progresses, the toroidal bubble expands continuously causing a funnel-shaped bubble with protrusion pointing to the downward direction, as shown in frames (e) and (f). In Fig. 9, the simulation shows qualitatively good agreement with the previous experimental and numerical results [10,18,20,21,25,28,49] in the terms of bubble shapes, where the dynamics of bubble collapse are well predicted near a solid wall.

Figure 10 features the bubble shapes with pressure contours and velocity vectors during the expansion phase [see frames (a)–(c)], the final stages of the collapse phase [see

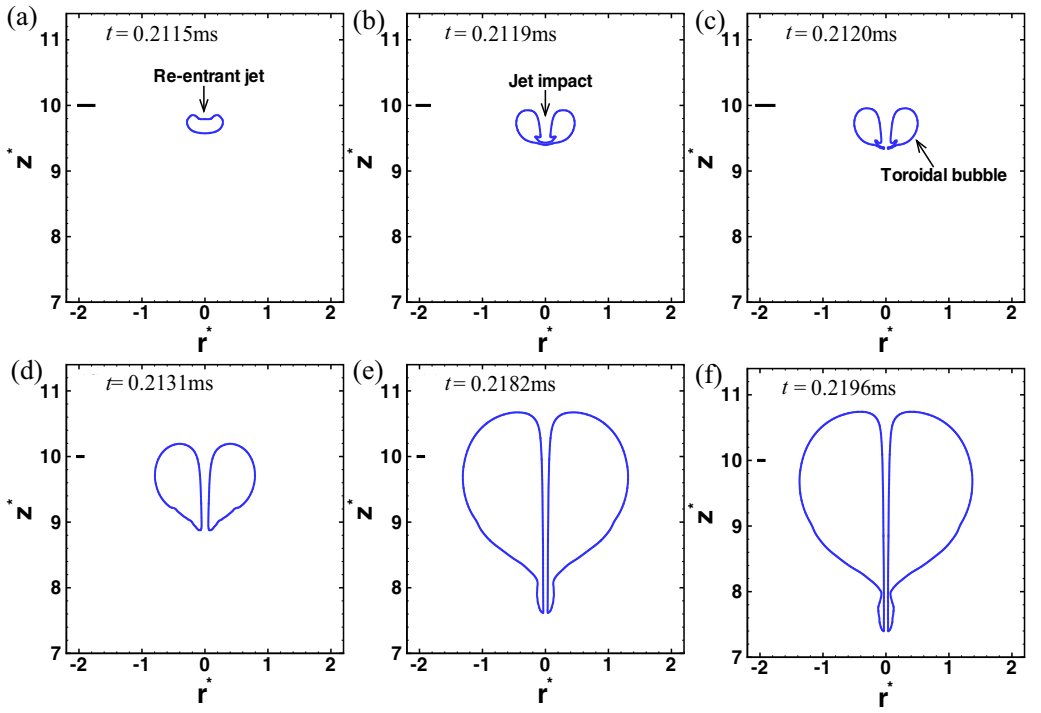

FIG. 9. Snapshots of the evolution of the bubble shapes during the rebound phase (second expansion phase). Here, the dimensionless time t^* can be written as (a) 0.11.75, (b) 11.77, (c) 11.78, (d) 11.84, (e) 12.12, and (f) 12.22.

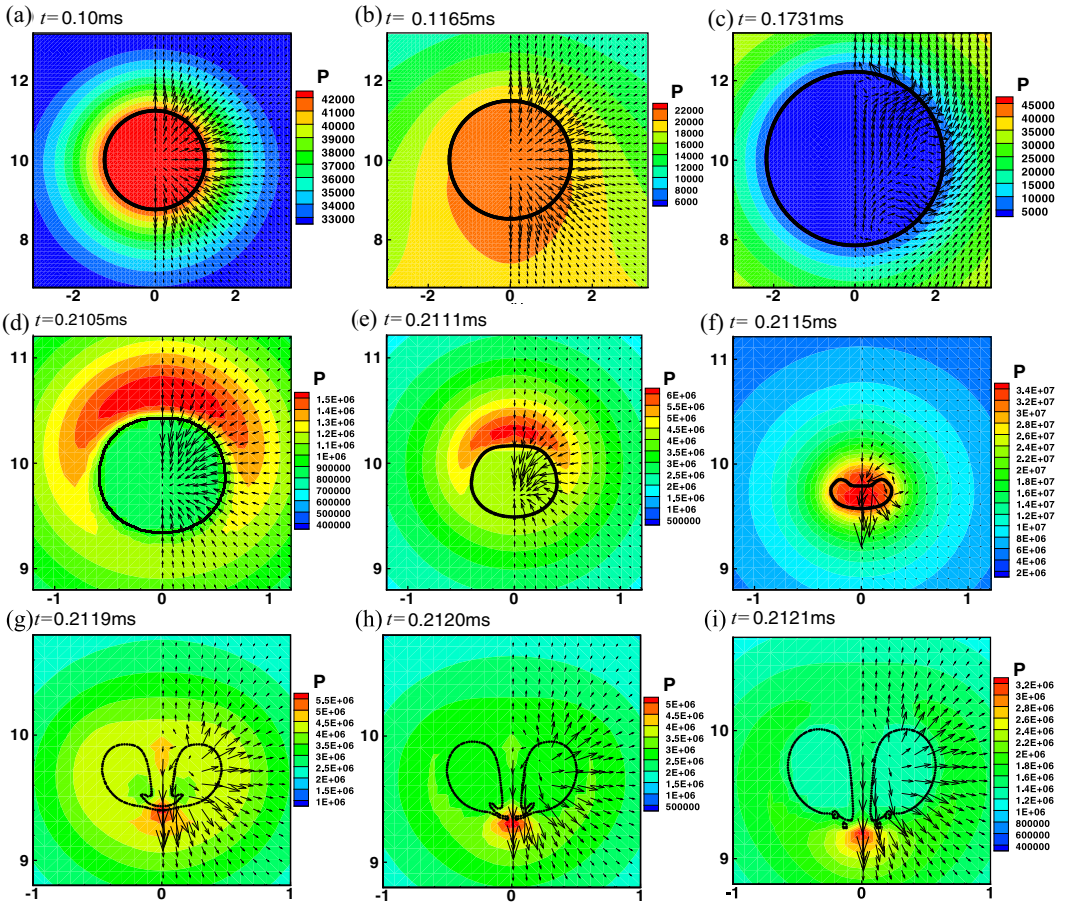

FIG. 10. Bubble interface with pressure contours and velocity vectors during (a)–(c) first expansion phase, (d)–(f) first collapse phase, and (g)–(i) early stages of rebound phase under the same conditions as in Fig. 7.

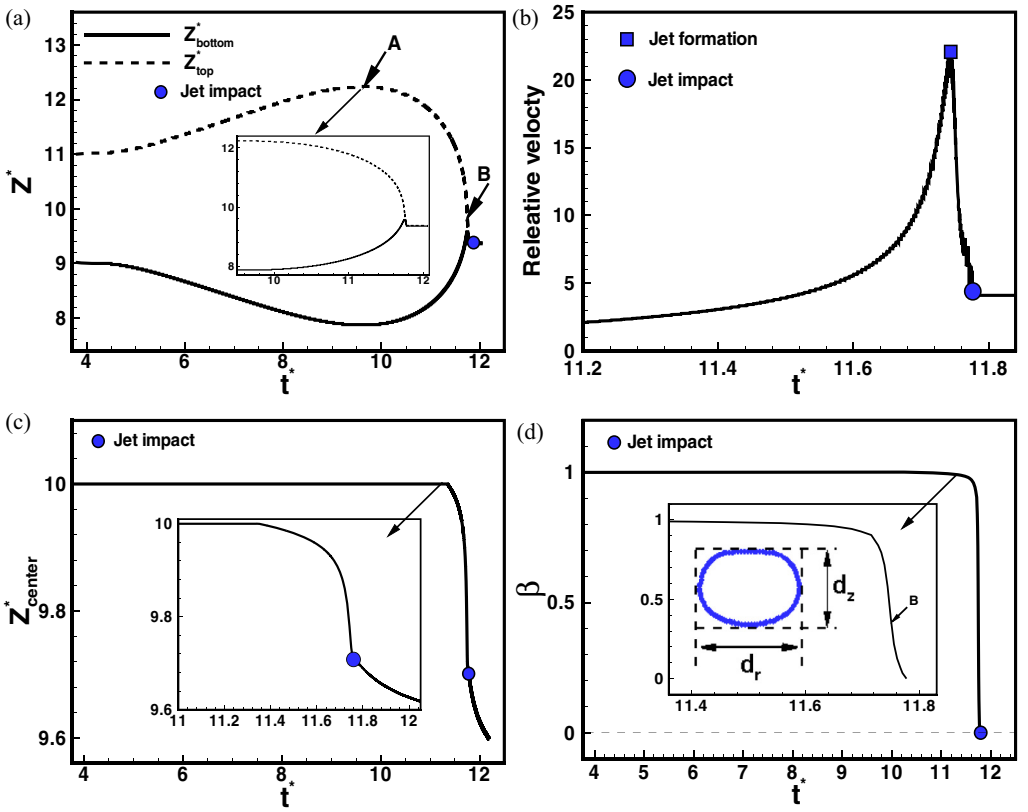

FIG. 11. The time evolution of (a) the position of of the extremes of the bubble located on the symmetric axis of the computational geometry, (b) relative velocity of the top and bottom extremes of the bubble, (c) the center position of the bubble, and (d) the bubble aspect ratio, $\beta = \frac{d_z}{d_r}$. The input parameters are the same as in Fig. 7.

frames (d)–(f)], and the early stages of the rebound phase [see frames (g)–(i)]. It is clearly seen from frames 10(d)–10(f) that the formed high liquid pressure near the upper side of the bubble results in the deformations of the upper surface of the bubble. At the end of collapse phase, this high liquid pressure region involves the formation of a re-entrant jet. Subsequently, the formed re-entrant liquid jet flows along the axial region and the jet completely penetrates through the bubble generating into two sub-bubbles. It is observed that the snapshots, reported in Fig. 10, allow us to describe fluid flows well during the volume oscillations and strong shape deformations.

Finally, as shown in Fig. 11, the time evolution of the position of the extremes of the bubble on the axisymmetric axis [Fig. 11(a)], the relative velocity of the top and bottom extremes of the bubble [Fig. 11(b)], the bubble center position [Fig. 11(c)], and the bubble aspect ratio β [Fig. 11(d)] is highlighted. In Fig. 11(a), it can be observed that during the expansion phase the difference between the two extremes increases with time. However, during the collapse phase the difference between the two extremes decreases and the top extreme accelerates downwards. Eventually, the re-entrant jet formed at the top extreme at the end of the collapse phase ($t^* = 11.75$) penetrates through the bubble and arrives at the bottom extreme at the beginning stages of the rebound phase ($t^* > 11.75$). As a result, the jet impacts on the bottom side of the bubble (filled circle symbol). In Fig. 11(b), the relative velocity, which is taken to be positive value during the collapse phase and the beginning stages of the rebound phase, is shown. It can be found that the maximum value of the relative velocity (filled square) reaches near the end of the collapse phase, which signals the moment of jet formation. Then, the upper side of the bubble becomes pierced by the re-entrant jet very rapidly and the liquid jet impacts (filled circle) at the minimum relative velocity.

It is noticeable from Figs. 8, 9, and 11(c) that there is a coupling between the bubble volume oscillations with the displacement of the bubble center position with time leading to the migration of the bubble towards the inflow (bottom) plane. It is noted that the bubble moves progressively during the collapse phase. At the beginning stages in the rebound phase, the bubble moves rapidly. Furthermore, it is interesting to note from Fig. 11(d) that the bubble shape remains spherical during the expansion phase and the early stages of the collapse phase, for which the value of β is 1.0. However, the bubble begins to lose its sphericity ($\beta < 1.0$) when $t^* > 11.4$. Afterwards, the deformation of the bubble is more observed for $11.65 < t^* \leqslant 11.75$, and the shape of the bubble becomes an oblatelike shape with the range $0.95 < \beta \leqslant 0.37$. In this case, Fig. 11(b) also shows that for $11.75 < t^* < 11.8$, the value of β reaches a value of zero, which indicates that the nonspherical bubble is highly deformed leading to the breakup of the bubble.

The experimental observations reported by Rodríguez-Rodríguez, Casado-Chacón, and Fuster [9] seem to be

difficult for visualizing the dynamics of bubble shapes and the formation of a re-entrant liquid jet. With the problem of interest, based on the above discussion, the quantitative and qualitative results show the potential of the proposed approach to provide the physical understanding and make visibly evident the growth, collapse, and rebound of a bubble with dynamically deformed interfaces and topology changes. However, the proposed weakly compressible two-fluid flow model is not efficient to capture well the violent collapse of the bubble [9,49] at the final stages of the collapse phase [see Fig. 7(b)] and from the point B [see Fig. 7(a)] onwards, where the axisymmetry breaks. Moreover, the computed Mach number in the gas is high, $M_g \approx 0.3$, at the end of the collapse. In future, the extension of this method for three-dimensional compressible flows coupled with energy equations is essential to undertake the limitation of this problem.

C. Characterizing the interactions of two coaxial gas bubbles

For the problem of the mutual interaction between two bubbles in an unbounded incompressible liquid in response to variations in the ambient pressure, extensive theoretical models have been proposed in the regimes of linear oscillations [50–52], nonlinear oscillations [53–56], and references therein. Their studies have shown the translational motions of two oscillating bubbles due to the secondary Bjerknes force [57]. Most of the previous theoretical models of the oscillating two bubble system is based on the assumption of the spherically symmetrical pulsations at long distances, except for the work produced by Pelekasis and Tsamopoulos [54,55]. Pelekasis and Tsamopoulos [54,55] have shown the strong interaction between two nonspherical oscillating bubbles at small separation distances. However, a comprehensive theoretical explanation for understanding the highly nonlinear behavior of multiple bubbles associated with nonspherical pulsations in an unbounded liquid still has unexplored aspects. On the other hand, to the best of the author's knowledge, very few numerical studies [17,23,24] have been conducted revealing the mutual interaction between two oscillating bubbles in liquids. However, the methods proposed by the authors of the studies [17,23,24] can be used only for potential flows [17] or Stokes flows [23,24].

As with the previously examined numerical study of Chatzidai *et al.* [23] and Chatzidai, Dimakopoulos, and Tsamopoulos [24], the interaction of two coaxial bubbles subjected to pressure changes in the ambient liquid is revisited to assess the ability of the present proposed method. For this purpose, the simulations are performed within computational domain size $32R_{10} \times 32R_{10}$, shown in Fig. 12, where two bubbles of radii R_1 (uppermost bubble) and R_2 (lowermost bubble), densities ρ_{g1} and ρ_{g2} with the separation distance between the centers D, are immersed in liquid. The initial equilibrium radii of the uppermost and lowermost bubbles are R_{10} and R_{20}, respectively, and the initial equilibrium pressure of two bubbles are determined by $p_{g,\mathrm{ref},j0} = p_{\mathrm{atm}} + \frac{2\sigma}{R_{j0}}$, where $j = 1, 2$. Note that the gas densities ρ_{gj} for each bubble are calculated from Eq. (10). As reported by Chatzidai *et al.* [23], using length scale with R_{10}, pressure scale with σ/R_{10}, time scale with $(R_{10}^3\rho_l/\sigma)^{1/2}$, and velocity scale with $(\sigma/R_{10}\rho_l)^{1/2}$, one can obtain the dimensionless parameters as

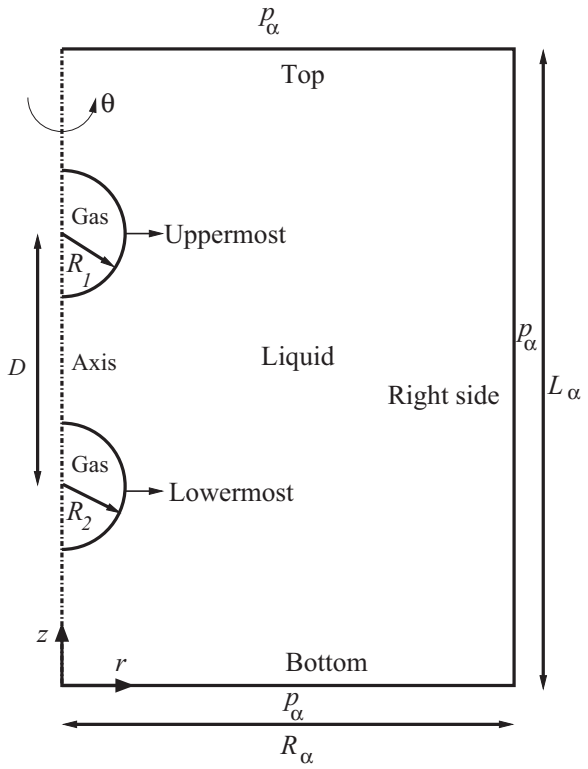

FIG. 12. Schematic view of the problem geometry used to consider the interaction of two coaxial bubbles in response to fast variations in the ambient pressure p_∞ in an axisymmetric computational domain on a (r, z) with independent θ.

the Ohnesorge number $\mathrm{Oh} = \mu_l/\sqrt{\rho_l R_{10}\sigma}$, the viscosity ratio $\lambda = \mu_g/\mu_l$, and the density ratio $\eta = \rho_g/\rho_l$.

With forcing $\varepsilon = 1$ and $\mathrm{Oh} = 0.1$, the numerical results of the dynamics of two interacting equal sized bubbles ($R_{10}^* = R_{20}^* = 1.0$) are shown in Figs. (13) and (14). In Fig. 13, the computed predictions are illustrated in terms of the time evolution of radial oscillations of the lowermost bubble R_2^*, the centers of each bubble $Z_{\mathrm{center},j}^*$, and the distance D^* between the centers and the velocities of each bubble U_j^*. Here, the instantaneous centers $Z_{\mathrm{center},j}$ and the instantaneous velocities U_j for each bubble are defined through

$$Z_{\mathrm{center},j} = \frac{\int_V (1-\alpha) z_j dV}{\int_V (1-\alpha) dV},$$

and

$$U_j = \frac{\int_V (1-\alpha)\mathbf{v_j}\cdot e_z dV}{\int_V (1-\alpha) dV},$$

where e_z is the unit vector in the vertical direction. In addition, the combined center of volume Z_c of the two oscillating bubbles [24] can be determined as

$$Z_c = \frac{Z_{\mathrm{center},1}V_1 + Z_{\mathrm{center},2}V_2}{V_1 + V_2},$$

where V_1 is the volume of the uppermost bubble and V_2 is the volume of the lowermost bubble. To test the accuracy of the present approach, the predicted result of R_2^*, shown in Fig. 13(a), is compared with the numerical data obtained from Chatzidai *et al.* [23]. The comparison reveals a very

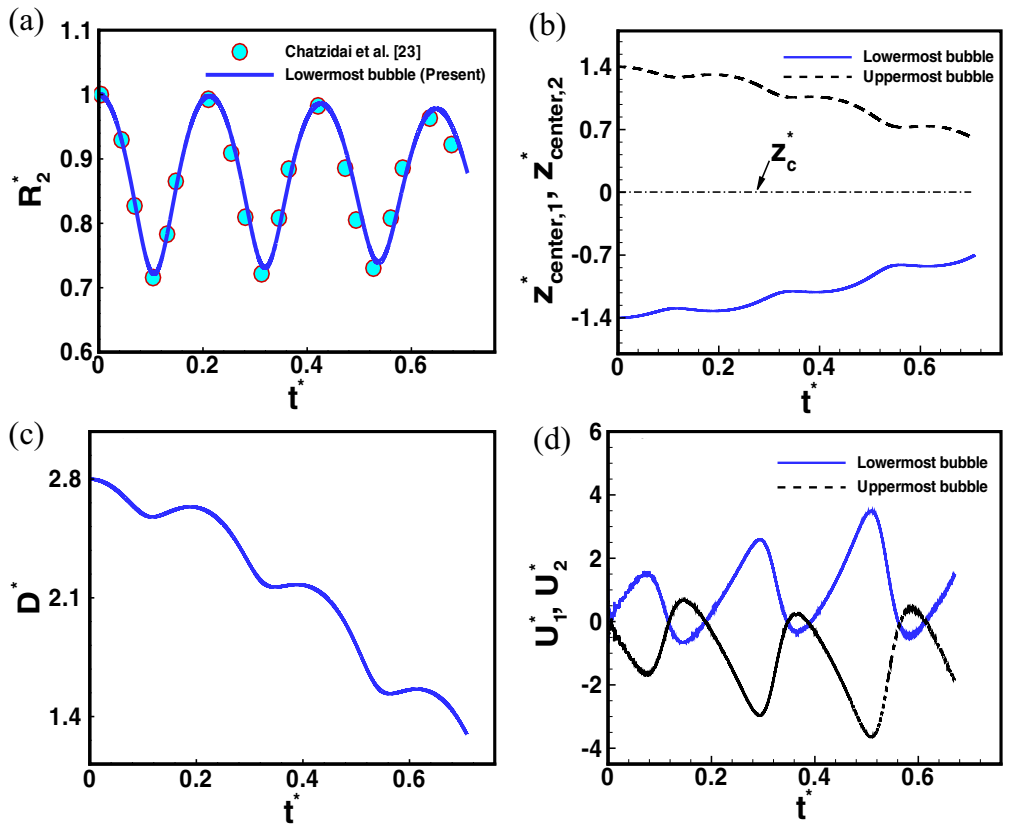

FIG. 13. (a) Comparison of the present computed history of the equivalent radius of the lowermost bubble R_2^* with the numerical result of Chatzidai *et al.* [23]. The time evolution of (b) $Z^*_{\text{center},1}$, $Z^*_{\text{center},2}$ and Z_c^*, (c) D^*, and (d) U_1^* and U_2^*. The pertinent input parameters are $p^*_{\text{atm}} = 100$, $\varepsilon = 1$, $\gamma = 1.4$, $R^*_{10} = R^*_{20} = 1.0$, $D^*(0) = 2.8$, $\text{Oh} = 0.1$, $\lambda = 3.652 \times 10^{-4}$, and $\eta_{\text{init}} = 10^{-3}$. Here, in (b) and (d) the solid line is for the lowermost bubble and the dashed line for the uppermost bubble.

good agreement resulting in a maximum error of about 2.0% relative to the those of Chatzidai *et al.* [23]. Furthermore, it appears that the amplitude of radial oscillations decreases slowly with time because of the effect of liquid viscosity (moderate Oh). Note that the time evolution of R_1^* (uppermost bubble) follows exactly the same way because of symmetry and equal sized bubbles (not shown here).

It is noteworthy that the volume oscillations of each bubble induced by a step change in pressure cause translational motions of two bubbles along their axis of symmetry as shown in Figs. 13(b) and 13(d). Figure 13(b) shows that the two centers of each bubble oscillate and keep approaching each other with time with a force known as secondary Bjerknes force [57]. The classical secondary Bjerknes theory in the linear regime of oscillations predicts that when the forcing frequency is greater or less than the natural frequencies of both bubbles the bubble pairs are seen to pulsate in phase and always attract, otherwise repulsive forces persuade. Here, the natural frequency [1,6] is defined as $\omega_0 = \sqrt{\frac{3\gamma p_{\text{atm}}}{\rho_l R_0^2} + \frac{(3\gamma-1)2\sigma}{\rho_l R_0^3}}$. In the present case, the forcing frequency is zero, $\omega_f^* = 0$, which is below the resonance frequencies of both bubbles ($\omega^*_{10}/2\pi = \omega^*_{20}/2\pi = 3.29$). As a result, based on linear theory, the two bubbles should therefore attract each other. This is indeed observed in Fig. 13. Furthermore, it is interesting to point out from this figure that the contraction phases of two bubbles develop attractive forces and the bubbles approach each other, whereas at the expansion phases, the force is repulsive and the bubbles move away from each other, the reason being nonlinear interactions [50,53]. Interestingly, this nonlinear effect makes net attraction between the two bubbles which results in the accelerating motion of the bubbles, and subsequently, coalescence can be observed (see Fig. 15). In addition, Fig. 13(b) also illustrates that the combined center Z_c^* remains at zero with time due to symmetry. Regarding the verifications, the numerical predictions of Figs. 13(b)–13(d) show qualitatively similar behavior to the results of Chatzidai, Dimakopoulos, and Tsamopoulos [24] and Oguz and Prosperetti [53].

Figure 14 reports the snapshots of the shape of two volume oscillating bubbles with pressure contour and velocity field at four different instants of dimensionless time. This figure shows that bubbles undergo nonspherical deformations and at the same time two bubbles approach each other with time. Finally, the two interacting bubbles merge coaxially with each other and an oscillating compound bubble is formed as shown in Fig. 15 which additionally demonstrates the advantage of the CLVOF method. It is worth noting from Fig. 14 that the values of the aspect ratio β in frames a and b are approximately 1.04 and 1.05, respectively, which correspond to prolate bubble shapes. Moreover, the bubbles attain oblate shapes, $\beta \approx 0.97$ and ≈ 0.85, as shown in frames (c) and (d). The behavior of the numerical simulation for the

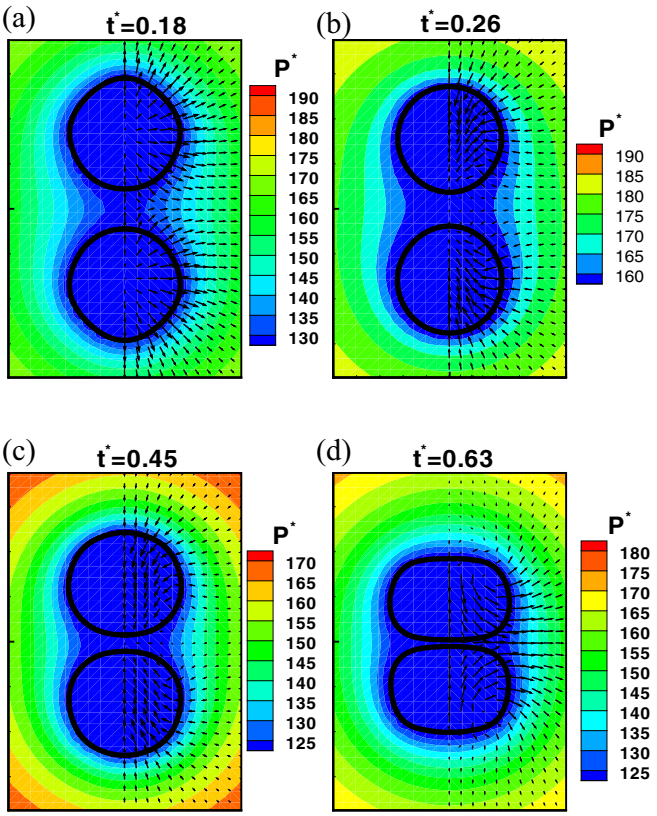

FIG. 14. Bubble shapes with pressure contours and velocity vectors during the interactions of two equal sized bubbles with the same parameters as in Fig. 13. Here, (a) and (d) expansion phase, and (b) and (c) contraction phase.

temporal evolution of bubble shapes agrees fairly well with the computations of Chatzidai *et al.* [23].

Next, the simulation results of the interactions between two unequal sized bubbles having equilibrium radii of $R^*_{10} = 1$ ($f^*_{10} = \omega^*_{10}/2\pi = 3.29$) and $R^*_{20} = 0.7$ ($f^*_{20} = \omega^*_{20}/2\pi = 4.71$) are presented in Fig. 16 using the same other parameters as in Fig. 13. It is observed that two radial oscillating bubbles [see Fig. 16(a)] move towards each other due to a mutual attraction force [see in Figs. 16(b)–16(d)]. The predicted results agree qualitatively with the classical secondary Bjerknes theory. Interestingly, it can be noted from Fig. 16(b) that the combined center of volume, Z^*_c, fluctuates with time and remains always positive. This clearly reveals that the bigger bubble (uppermost bubble) has a strong effect on the translational motion of the smaller one (lowermost bubble) and the smaller bubble moves faster than that of the bigger one [see also Fig. 16(d)]. The similar observations of two interacting unequal sized bubbles are reported by [53,55].

Finally, two numerical results of a bubble pair having equilibrium radii of $R^*_{10} = 1$ ($f^*_{10} = \omega^*_{10}/2\pi = 3.29$) and $R^*_{20} = 0.7$ ($f^*_{20} = \omega^*_{20}/2\pi = 4.71$) under the applied far-field oscillatory pressure with a pressure value $p_\infty = p_{\rm atm}(1 + \varepsilon \cos\omega_f t)$ are presented in Figs. 17 and 18. In both examples, the bubbles are forced with $\varepsilon = 0.3$ and a frequency of $f^*_f = \omega^*_f/2\pi = 4.07$, and the unequal sized bubbles are initially separated between the centers with $D^*(0) = 4.0$ as in Fig. 17 and $D^*(0) = 2.8$ as in Fig. 18. The other dimensionless parameters are the same as used in Fig. 13. It can be noted that the forcing frequency is between the natural frequency of either bubble, i.e., $f^*_{10} < f^*_f < f^*_{20}$. According to the linear theory of Bjerknes forces, the bubbles should repel each other. Qualitatively, this is evident from Fig. 17. In Fig. 17(c), it is observed that initially a mutual attraction force is developed, but for $t^* > 0.6$ the two bubbles move away from each other through the oscillatory translational motion caused by mutual repulsion force. Decreasing the initial separation distance to $D^*(0) = 2.8$, an interesting phenomenon of the dynamics of two interacting bubbles can be seen in Fig. 18. This figure illustrates a strong mutual attraction of bubbles and the bubbles are moving towards each other, which is in contrast with the linear theory. This result occurs due to the strong nonlinear effects on the mutual interaction of the bubble pairs, the reason being that the natural frequencies of two interacting bubbles change with decreasing D^* [56]. As a result, in this case, the nonlinear effect may switch the direction of force as observed in Figs. 17 and 18. Interestingly, Oguz and Prosperetti [53] also reported the shift from repulsive to attractive due to the change of the amplitude of the forcing pressure ε. In this investigation, the numerical predictions may help in the physical modeling of the acoustic response of stable multiple bubbles subjected to a periodic acoustic excitation.

IV. CONCLUDING REMARKS

A numerical method based on a weakly compressible two-fluid flow model with a high density ratio is proposed to predict the interaction of a bubble with the fast pressure variations in the ambient liquid. In the method, a single-fluid continuum formulation of the axisymmetric Navier-Stokes equations, which takes into account the surface tension effects, and a pressure-based algorithm are presented in the framework of the Eulerian finite difference scheme on structured grids, where the interface is captured by means of a coupled level set and volume of fluid (CLSVOF) method. This method in turn

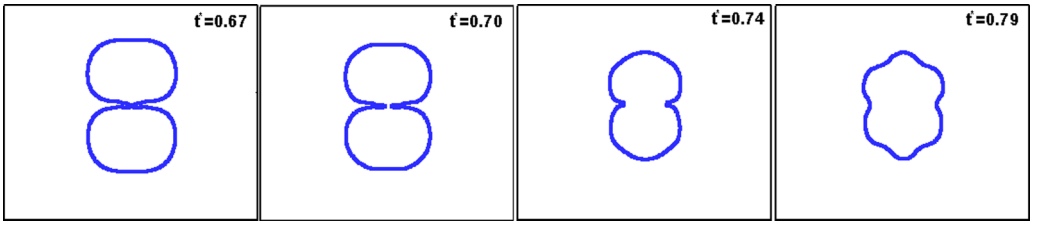

FIG. 15. Time instant of the coalescence of the two coaxial bubbles and an oscillating compound bubble formation with the same parameters as in Fig. 13.

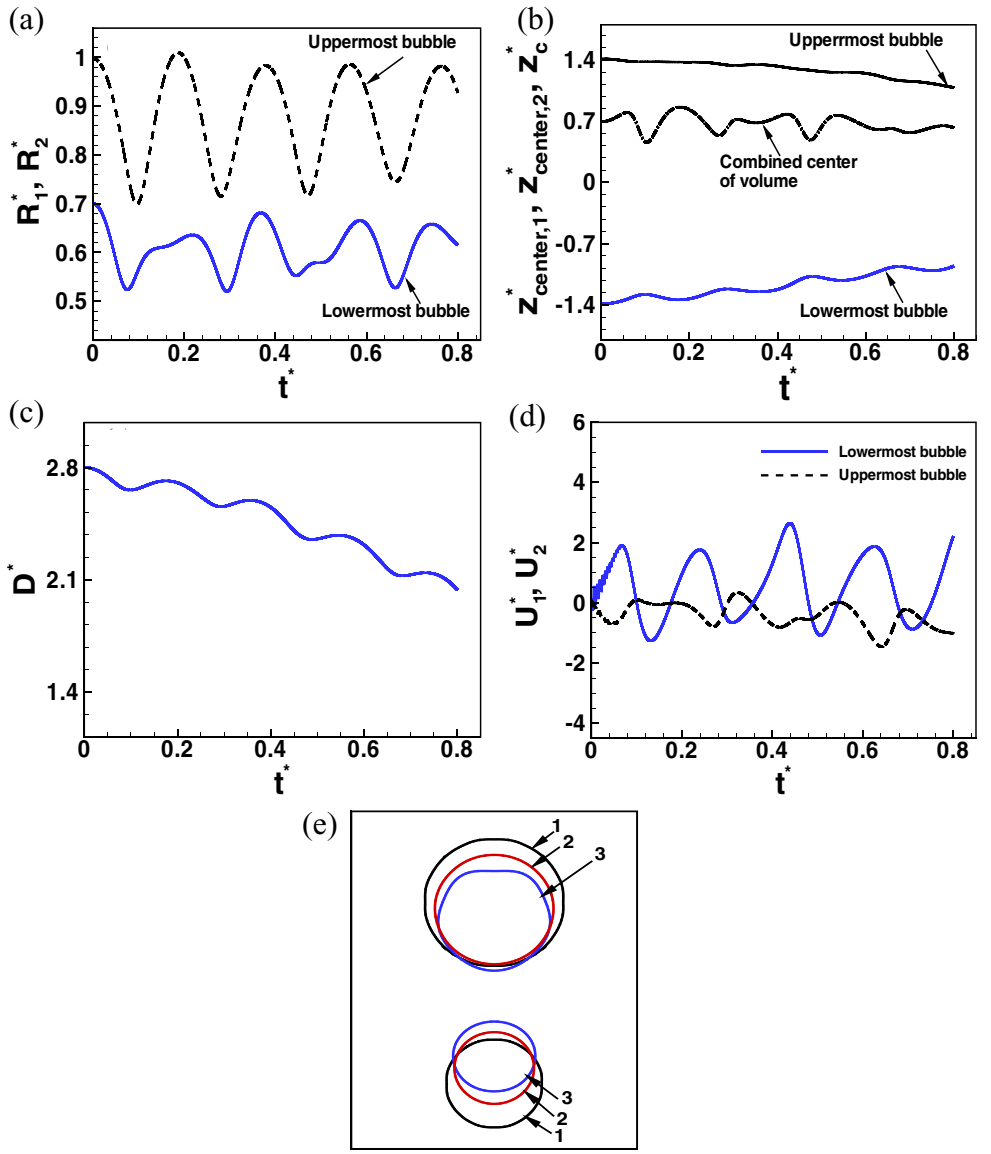

FIG. 16. (a) The computed history of the equivalent radius of two oscillating bubbles. The time evolution of (b) $Z^*_{\text{center},1}$, $Z^*_{\text{center},2}$ and Z^*_c, (c) D^*, (d) U_1^* and U_2^*, and (e) bubble shapes at times t^* (1) 0.02, (2) 0.44, and (3) 0.68, under a step change in surrounding pressure ($f_f^* = 0$). The input parameters are $p^*_{\text{atm}} = 100,\ \varepsilon = 1,\ \gamma = 1.4,\ R^*_{10} = 1,\ R^*_{20} = 0.7,\ D^*(0) = 2.8,\ \text{Oh} = 0.1,\ \lambda = 3.652 \times 10^{-4}$ and $\eta_{\text{init}} = 10^{-3}$.

leads to conserve mass and estimate the interface geometric properties very accurately, although the method presented here is applicable in the limit of low Mach number liquid-gas flows. In the low Mach number regime with moderately high pressure forcing frequencies and amplitude ratios, numerical results are provided by simulating three problems to demonstrate the predictive capabilities of the presented two-phase flow model. One notable advantage of the current approach is that the thermodynamic gas pressure is evaluated through the mass conservation of the gas phase also (see Sec. II C), which is used to accurately predict the density variation in the single-fluid formulation.

In a first problem, the accuracy of the proposed method is assessed by comparing with a reference solution of Rayleigh-Plesset equation. In a second problem, the method is implemented to deal with the dynamics of the growth and subsequent collapse of a bubble in an unbounded liquid medium. Comparison with the experimental results shows a very good agreement with respect to the evolution of the bubble radius. However, due to the axisymmetric flow assumptions, the simulations for this problem show a limitation when the violent collapse occurs. Nevertheless, the method is able to capture the collapsed induced formation of a re-entrant jet and bubble break up nonspherically into the formation of toroidal bubble during the early stages of the bubble rebound phase, corroborating the qualitative agreement with the previous investigations. Finally, the potential of the method is further shown by computing the challenging problem on the dynamics of a pair of the nonlinear interacting bubbles in liquid. The simulations demonstrate encouraging results in terms of radial oscillations, nonspherical deformations, and translational motions. It is unexpectedly shown that the nonlinear interactions of the two unequal sized bubbles switch the direction of the mutual force upon decreasing the initial separation distance

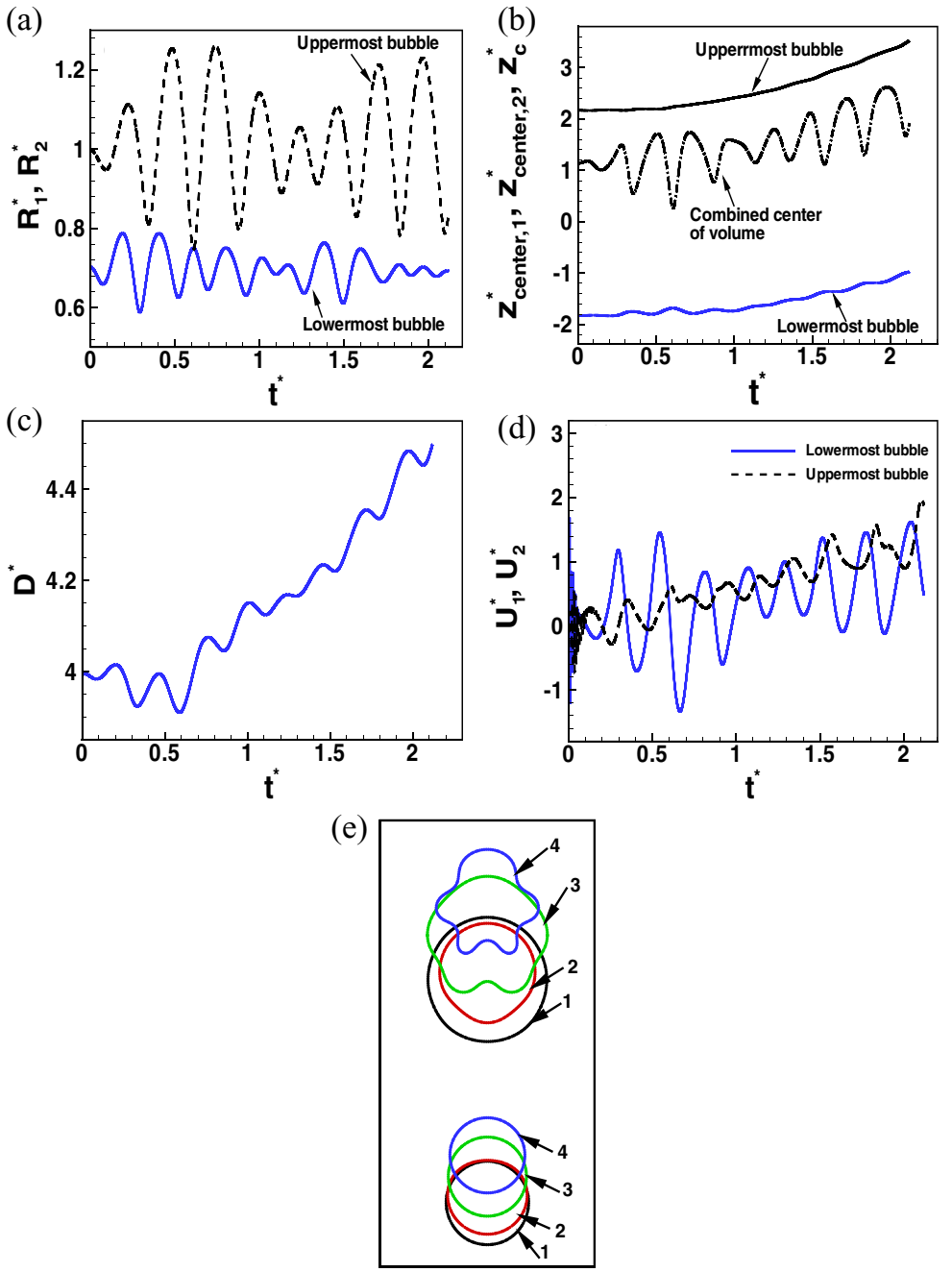

FIG. 17. (a) The computed history of the equivalent radius of two oscillating bubbles. The time evolution of (b) $Z^*_{\text{center},1}$, $Z^*_{\text{center},2}$, (c) D^*, (d) U_1^* and U_2^*, and (e) bubble shapes at times t^* (1) 0.22, (2) 0.85, (3) 1.64, and (4) 2.12 under an oscillatory pressure field ($f_f^* = 4.07$). The pertinent input parameters are $p^*_{\text{atm}} = 100$, $\varepsilon = 0.3$, $\gamma = 1.4$, $R^*_{10} = 1$, $R^*_{20} = 0.7$, $D^*(0) = 4.0$, $\text{Oh} = 0.1$, $\lambda = 3.652 \times 10^{-4}$, and $\eta_{\text{init}} = 10^{-3}$.

between the bubble centers, which is contradictory to the prediction of the linear theory of the classical secondary Bjerknes force. It is worth noting that the computations of two interacting bubble pairs with the variation of the ambient pressure are attempted by using the current two-phase flow model in the framework of the interface capturing method. Future work aims to investigate the translational dynamics of microbubbles or encapsulated microbubbles [22] due to the primary Bjerknes force [57,58] under the action of acoustic pulses. This study could be of great importance in ultrasound medical therapy [13,14].

In summary, the computed results, which are confirmed after performing grid and time-step refinement studies, ensure the ability of the proposed two-phase flow model as a promising alternative tool for the simulations of bubble oscillating in liquids under applied forcing pressure.

ACKNOWLEDGMENTS

The author is indebted to Prof. J. Rodríguez-Rodríguez in the Fluid Mechanics Group at Carlos III University of

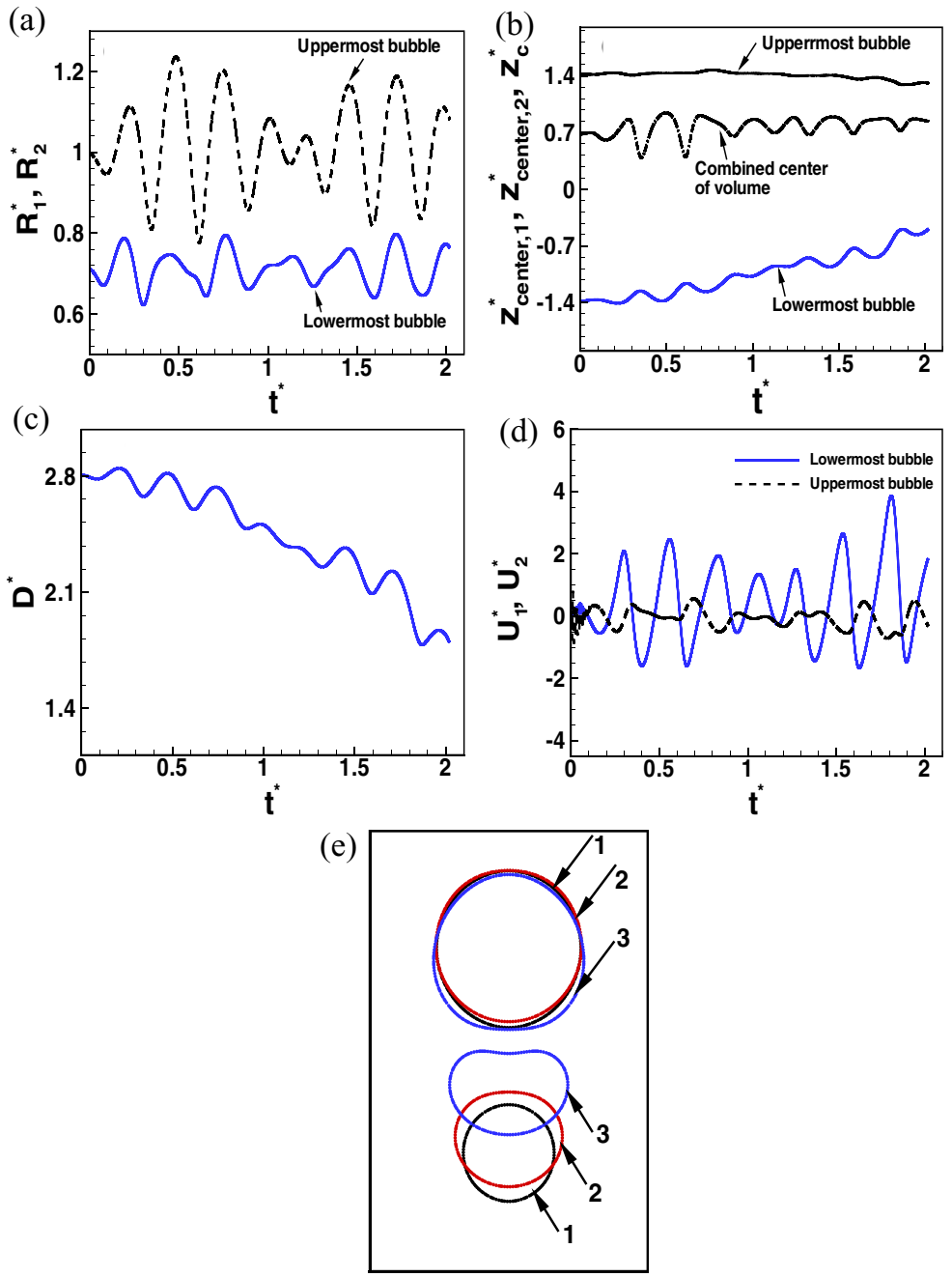

FIG. 18. (a) The computed history of the equivalent radius of two oscillating bubbles. The time evolution of (b) $Z^*_{\text{center},1}$, $Z^*_{\text{center},2}$ and Z^*_c, (c) D^*, (d) U_1^* and U_2^*, and (e) bubble shapes at times t^* (1) 0.27, (2) 0.82, and (3) 2.02 under an oscillatory pressure field ($f_f^* = 4.07$). The input parameters are $p^*_{\text{atm}} = 100,\ \varepsilon = 0.3,\ \gamma = 1.4,\ R^*_{10} = 1,\ R^*_{20} = 0.7,\ D^*(0) = 2.8\,\text{Oh} = 0.1,\ \lambda = 3.652 \times 10^{-4}$, and $\eta_{\text{init}} = 10^{-3}$.

Madrid for his insightful comments and discussion. The author acknowledges the financial support from the Spanish Ministry of Economy and Competitiveness through Grant No. DPI2014-59292-C3-1, partly funded through European Funds. In addition, the author, who is currently working at the University of Warwick, wishes to acknowledge the financial support of the Leverhulme Trust (Research Project Grant) and the EPSRC (Grants No. EP/N016602/1, No. EP/P020887/, and No. EP/P031684/1). I would like to express my sincere gratitude to Prof. Gautam Biswas at IIT Guwahati (India) and Prof. A. M. Leshansky at Techion-IIT (Israel) for their constant support and encouragement. I am thankful to the anonymous referees for their comments which led to an improvement of the manuscript.

APPENDIX: ADVECTION EQUATION OF THE VOLUME FRACTION

In a single-fluid model, the continuity equations of gas and liquid phases with no phase change, further, can be written in a separate form given by

$$\frac{\partial[\,(1-\alpha)\rho_g]}{\partial t} + \nabla\cdot[\,(1-\alpha)\rho_g\mathbf{v}] = 0, \qquad \text{(A1)}$$

$$\frac{\partial \alpha \rho_l}{\partial t} + \nabla \cdot (\alpha \rho_l \mathbf{v}) = 0. \tag{A2}$$

By recalling Sec. II, as ρ_l is constant, the above two equations can be read

$$\frac{\partial (1-\alpha)}{\partial t} + \nabla \cdot [(1-\alpha)\mathbf{v}] = -\frac{(1-\alpha)}{\gamma_g p}\frac{Dp}{Dt}, \tag{A3}$$

$$\frac{\partial \alpha}{\partial t} + \nabla \cdot (\alpha \mathbf{v}) = 0. \tag{A4}$$

Then, by adding the above two equations, the divergence of the velocity field for weakly compressible gas-liquid flows can be expressed as

$$\nabla \cdot \mathbf{v} = -\frac{(1-\alpha)}{\gamma_g p}\frac{Dp}{Dt}, \tag{A5}$$

which is nonzero. It is noted that Eq. (A5) is the same as the continuity Eq. (15), and Eq. (A4) is the advection equation of the volume fraction to preserve the mass of two-phase flows with the CLSVOF method in a low Mach number regime, as pointed out before by Heyns *et al.* [37] with the VOF approach.

[1] M. S. Plesset and A. Prosperetti, Annu. Rev. Fluid Mech. **9**, 145 (1977).
[2] C. E. Brennen, *Cavitation and Bubble Dynamics* (Oxford University Press, New York, 1995).
[3] Z. C. Feng and L. G. Leal, Annu. Rev. Fluid Mech. **29**, 201 (1997).
[4] Y. Hao and A. Prosperetti, Phys. Fluid **11**, 1309 (1999).
[5] M. Versluis, D. E. Goertz, P. Palanchon, I. V. Heitman, S. M. van der Meer, B. Dollet, N. D. Jong, and D. Lohse, Phys. Rev. E **82**, 026321 (2010).
[6] T. G. Leighton, *The Acoustic Bubble* (Academic Press, London, 1994).
[7] L. Rayleigh, Philos. Mag. **34**, 94 (1917).
[8] C. E. Brennen, J. Fluid Mech. **472**, 153 (2002).
[9] J. Rodríguez-Rodríguez, A. Casado-Chacón, and D. Fuster, Phys. Rev. Lett. **113**, 214501 (2014).
[10] J. R. Blake and D. C. Gibson, Annu. Rev. Fluid Mech. **19**, 99 (1987).
[11] C. D. Ohl, M. Arora, R. Ikink, N. D. Jong, M. Versluis, M. Delius, and D. Lohse, Biophys. J. **91**, 4285 (2006).
[12] J. R. Lindner, Nat. Rev. Drug Discovery **3**, 527 (2004).
[13] E. C. Unger, E. Hersh, M. Vannan, T. O. Matsunaga, and T. McCreery, Prog. Cardiovasc. Dis. **44**, 45 (2001).
[14] J. Rodríguez-Rodríguez, A. Sevilla, C. Martnez-Bazn, and J. M. Gordillo, Annu. Rev. Fluid Mech. **47**, 405 (2015).
[15] S. Popinet, Annu. Rev. Fluid Mech. **50**, 49 (2018).
[16] R. Saurel and C. Pantano, Annu. Rev. Fluid Mech. **50**, 105 (2018).
[17] J. R. Blake, P. B. Robinson, A. Shima, and Y. Tomita, J. Fluid Mech. **255**, 707 (1993).
[18] M. Lee, E. Klaseboer, and B. C. Khoo, J. Fluid Mech. **570**, 407 (2007).
[19] M. S. Pleseet and Chapman, J. Fluid Mech. **47**, 283 (1971).
[20] Q. Wang, J. Fluid Mech. **745**, 509 (2014).
[21] A. M. Zhang, S. Li, and J. Cui, Phys. Fluid **27**, 062102 (2015).
[22] Y. Liu, K. Sugiyama, S. Takagi, and Y. Matsumoto, Phys. Fluid **23**, 041904 (2011).
[23] N. Chatzidai, A. Giannousakis, Y. Dimakopoulos, and J. Tsamopoulos, J. Comput. Phys. **228**, 1980 (2009).
[24] N. Chatzidai, Y. Dimakopoulos, and J. Tsamopoulos, J. Fluid Mech. **673**, 513 (2011).
[25] S. Popinet and S. Zaleski, J. Fluid Mech. **464**, 137 (2002).
[26] Y. Hao and A. Prosperetti, J. Comput. Phys. **196**, 126 (2004).
[27] X.-D. Liu, R. P. Fedkiw, and K. Myungjoo, J. Comput. Phys. **160**, 151 (2000).
[28] M. Sussman, J. Comput. Phys. **187**, 110 (2003).
[29] M. Sussman and E. G. Puckett, J. Comput. Phys. **162**, 301 (2000).
[30] D. Gerlach, G. Tomar, G. Biswas, and F. Durst, Int. J. Heat Mass Transfer **49**, 740 (2006).
[31] I. Chakraborty, G. Biswas, and P. S. Ghoshdastidar, Int. J. Heat Mass Transfer **58**, 240 (2013).
[32] S. Osher and J. A. Sethian, J. Comput. Phys. **79**, 12 (1988).
[33] C. W. Hirt and B. D. Nichols, J. Comput. Phys. **39**, 201 (1981).
[34] V. Daru, P. L. Quèrè, M.-C. Duluc, and O. L. Maître, J. Comput. Phys. **229**, 8844 (2010).
[35] B. Koren, M. R. Lewis, E. H. van Brummelen, and B. van Leer, J. Comput. Phys. **181**, 654 (2002).
[36] S. Y. Kadioglu, M. Sussman, S. Osher, J. P. Wright, and M. Kang, J. Comput. Phys. **209**, 477 (2005).
[37] J. A. Heyns, A. G. Malan, T. M. Harms, and O. F. Oxtoby, J. Comput. Phys. **240**, 145 (2013).
[38] G. Huber, S. Tanguy, J.-C. Bera, and B. Gilles, J. Comput. Phys. **302**, 439 (2015).
[39] B. Duret, R. Canu, J. Reveillon, and F. X. Demoulin, Int. J. Multiphase Flow **108**, 42 (2018).
[40] J. U. Brackbill, D. B. Kothe, and C. Zemach, J. Comput. Phys. **100**, 335 (1992).
[41] A. Prosperetti, L. A. Crum, and K. W. Commander, J. Acoust. Soc. Am. **83**, 502 (1987).
[42] F. H. Harlow and J. E. Welch, Phys. Fluid **8**, 2182 (1965).
[43] Y. C. Chang, T. Y. Hou, B. Merriman, and S. Osher, J. Comput. Phys. **124**, 449 (1996).
[44] K. Goda, J. Comput. Phys. **30**, 76 (1979).
[45] H. A. Van der Vorst, SIAM J. Sci. Stat. Comput. **13**, 631 (1992).
[46] E. G. Puckett, A. S. Almgren, J. B. Bell, D. L. Marcus, and W. J. Rider, J. Comput. Phys. **130**, 269 (1997).
[47] J. E. Pilliod and E. G. Puckett, J. Comput. Phys. **199**, 465 (2004).
[48] M. Sussman, P. Smereka, and S. Osher, J. Comput. Phys. **114**, 146 (1994).
[49] M. M. Daou, E. Igualada, H. Dutilleul, J. Rodríguez-Rodríguez, S. Zaleski, and D. Fuster, AIChE J. **63**, 2483 (2017).

[50] E. A. Zabolotskaya, Sov. Phys. Acoust. **30**, 365 (1984).
[51] A. A. Doinikov and S. T. Zavtrak, Phys. Fluid **7**, 1923 (1995).
[52] T. Barbat, N. Ashgriz, and C. H. Liu, J. Fluid Mech. **389**, 137 (1999).
[53] H. N. Oguz and A. Prosperetti, J. Fluid Mech. **218**, 143 (1990).
[54] N. A. Pelekasis and J. A. Tsamopoulos, J. Fluid Mech. **254**, 467 (1993).
[55] N. A. Pelekasis and J. A. Tsamopoulos, J. Fluid Mech. **254**, 501 (1993).
[56] A. Harkin, T. J. Kaper, and A. Nadim, J. Fluid Mech. **445**, 377 (2001).
[57] V. F. K. Bjerknes, *Fields of Force* (Columbia University Press, New York, 1906).
[58] E. Igualada, A. Medina, P. Vega, and J. Rodríguez-Rodríguez, J. Fluid Mech. **836**, 649 (2018).